AFRL-AFOSR-VA-TR-2023-0373

Multi-Stream Near-Wall Turbulence Dynamics

Glauser, Mark
SYRACUSE UNIVERSITY
900 S CROUSE AVE
SYRACUSE, NY, 13244
USA

06/21/2023
Final Technical Report

Air Force Research Laboratory
Air Force Office of Scientific Research
Arlington, Virginia 22203
Air Force Materiel Command

REPORT DOCUMENTATION PAGE

PLEASE DO NOT RETURN YOUR FORM TO THE ABOVE ORGANIZATION.

1. REPORT DATE	2. REPORT TYPE	3. DATES COVERED	
20230621	Final	START DATE 20190201	END DATE 20221130

4. TITLE AND SUBTITLE
Multi-Stream Near-Wall Turbulence Dynamics

5a. CONTRACT NUMBER	5b. GRANT NUMBER	5c. PROGRAM ELEMENT NUMBER
	FA9550-19-1-0081	61102F
5d. PROJECT NUMBER	**5e. TASK NUMBER**	**5f. WORK UNIT NUMBER**

6. AUTHOR(S)
Mark Glauser

7. PERFORMING ORGANIZATION NAME(S) AND ADDRESS(ES)
SYRACUSE UNIVERSITY
900 S CROUSE AVE
SYRACUSE, NY 13244
USA

8. PERFORMING ORGANIZATION REPORT NUMBER

9. SPONSORING/MONITORING AGENCY NAME(S) AND ADDRESS(ES)	10. SPONSOR/MONITOR'S ACRONYM(S)	11. SPONSOR/MONITOR'S REPORT NUMBER(S)
Air Force Office of Scientific Research 875 N. Randolph St. Room 3112 Arlington, VA 22203	AFRL/AFOSR RTA1	AFRL-AFOSR-VA-TR-2023-0373

12. DISTRIBUTION/AVAILABILITY STATEMENT
A Distribution Unlimited: PB Public Release

13. SUPPLEMENTARY NOTES

14. ABSTRACT
The experiments and Large Eddy Simulations described herein focus on a Multi-Aperture Rectangular Single Expansion Ramp Nozzle (MARS). The MARS flow field consists of two streams separated by a splitter plate; an (upper) supersonic core stream (Mach = 1.6) expanding through a single-sided expansion ramp and a (lower) bypass stream (Mach = 1) bounded by an aft deck at the bottom. Frequency dependent POD using experimentally validated LES data, indicates that the splitter plate is a highly sensitive region that remarkably alters the dynamics of the flow downstream of the trailing edge due to a two dimensional von Kármán-like shedding instability. This instability is shown to be potentially responsible for impairing the effectiveness of the bypass stream as a thermal and acoustic barrier between the core jet and the aft deck, and also to be exhibiting a global influence on the flow due to interaction with the shock train. To reduce these deleterious effects, the eigenspectrum obtained from linear stability is probed for unstable spanwise periodic disturbances and used to inspire surface modifications to the splitter plate trailing edge. The proposed chevron-like modifications have been employed both computationally and experimentally demonstrating their ability to excite three-dimensional instabilities in order to significantly reduce the growth of energy in the two-dimensional von Kármán shedding.

15. SUBJECT TERMS

16. SECURITY CLASSIFICATION OF:			17. LIMITATION OF ABSTRACT	18. NUMBER OF PAGES
a. REPORT U	b. ABSTRACT U	c. THIS PAGE U	UU	41

19a. NAME OF RESPONSIBLE PERSON	19b. PHONE NUMBER *(Include area code)*
GREGG ABATE	425-1779

Standard Form 298 (Rev.5/2020)
Prescribed by ANSI Std. Z39.18

Final Report: Multi-Stream Near-Wall Turbulence Dynamics

AFOSR Grant Number FA9550-19-1-0081
Period: 02/01/2019 – 11/30/2022

Mark Glauser and Jacques Lewalle
Syracuse University, Syracuse New York 13244
and
Datta V. Gaitonde
The Ohio State University, Columbus, Ohio 43210

Abstract

The experiments and Large Eddy Simulations described herein focus on a Multi-Aperture Rectangular Single Expansion Ramp Nozzle (MARS). The MARS flow field consists of two streams separated by a splitter plate; an (upper) supersonic core stream (Mach = 1.6) expanding through a single-sided expansion ramp and a (lower) bypass stream (Mach = 1) bounded by an aft deck at the bottom. Frequency dependent POD using experimentally validated LES data, indicates that the splitter plate is a highly sensitive region that remarkably alters the dynamics of the flow downstream of the trailing edge due to a two dimensional von Kármán-like shedding instability. This instability is shown to be potentially responsible for impairing the effectiveness of the bypass stream as a thermal and acoustic barrier between the core jet and the aft deck, and also to be exhibiting a global influence on the flow due to interaction with the shock train. To reduce these deleterious effects, the eigenspectrum obtained from linear stability is probed for unstable spanwise periodic disturbances and used to inspire surface modifications to the splitter plate trailing edge. The proposed chevron-like modifications have been employed both computationally and experimentally demonstrating their ability to excite three-dimensional instabilities in order to significantly reduce the growth of energy in the two-dimensional von Kármán shedding. The trailing edge of the splitter plate in the MARS experiments and simulations is modified to include the spanwise periodic perturbations, guided by the LES of the simple shear layer, and show a significant reduction in the strong high frequency tone observed in the baseline case, as discussed in Doshi et al. 2021a, Gist et al. 2021a and Doshi 2023. To simulate the nozzle with the wavy splitter plate being integrated into an existing airframe, tests have been conducted with three different aft deck geometries: a nominal length deck, half nominal, and no deck. PIV of the nominal configuration showed a slight change in the deflection angle of the jet plume. The differences for the half and no deck cases were less significant when compared to those results for the nominal splitter plate (non-wavy trailing edge). Preliminary experimental active control results, for all actuation cases, showed that the dominant frequency tone was shifted to a lower frequency and an additional reflected shock was formed in the near-field. Jets blowing at a 45 degree angle with respect to the core flow were shone to decrease the SPL of this tone by 8dB in addition to the reduction in frequency. Gist et al. 2022, Gist et al. 2021b, Doshi et al. 2021, Gist 2022, Doshi 2023 and Kelly et al 2023 summarize these efforts.

The LES Analysis of the Simple Shear Layer

At this point in the final report, we present the LES analysis of the simple shear layer given its importance in guiding the experiments and the LES of the full configuration. LES calculations for the full configuration with the wavy splitter plate for the nominal aft deck configuration are presented later in this final report.

Overview of the LES Analysis

The Large Eddy Simulation (LES) mean data of a flow past a splitter plate is analyzed using resolvent analysis with the objective of motivating a passive control strategy. The configuration of interest consists of two streams; a supersonic (Mach 1.23) upper stream and a sonic (Mach 1) lower stream, separated by a splitter plate of non-negligible thickness. Canonically, these two streams and the plate represent the supersonic multi-stream nozzle flow in an airframe-integrated variable-cycle engine architecture, with the upper stream being analogous to the power-producing core stream, and the lower stream being analogous to the bypass stream which shields the airframe from the thermal and acoustic loading of the core while providing some other design benefits. Numerical and experimental campaigns in previous studies have shown that this flow characteristically exhibits a two-dimensional vortex-shedding-like instability, which has a potentially detrimental first-order impact on performance. To gain insight into the instability mechanism, resolvent analysis is used to obtain the spatial structure of the optimal forcing of the mean flow. Modifications to the trailing edge of the plate, in the form of sinusoidal spanwise crests and troughs, are then introduced to interfere with this internal forcing mechanism and the resulting flows are simulated with LES. Proper Orthogonal Decomposition (POD) using snapshots of the LES data along the streamwise direction reveal a substantial increase in the rank of the modified flow, with a diminishing of the shedding instability as the spanwise wavenumber of the trailing-edge features is increased. Additionally, Dynamic Mode Decomposition (DMD) results reveal that the trailing-edge features induce a superposition of several resolvent response modes which rapidly decay downstream due to the non-linear action of turbulence.

Details of the Results of the LES Analysis

Previous efforts in the literature have addressed the vortex instability issue through passive flow control measures, specifically by modifying the splitter plate trailing edge (SPTE) since this is where the instability originates and subsequently grows. Ruscher et al. 2018 observed that replacing the flat splitter plate with a knife-edged plate changes the nature of the instability from vortex-shedding to a more tractable Kelvin-Helmholtz-like mechanism. Stack et al. 2019 explored the influence of the thickness of the splitter plate on the instability and observed that the sizes of the coherent structures scaled with the thickness of the plate. An interesting observation was that the structures formed with a one-tenth baseline thickness plate, showed no distinct shedding instability and had a minimal influence on the

rest of the flowfield. Although effective in changing the instability mechanism, thinning the plate is deleterious to its structural integrity, and hence other trailing edge modifications are explored here. The objective of the LES is therefore to employ high-fidelity simulations informed by linear techniques to guide changes to the SPTE geometry; the goal is to control the observed shedding instability without altering the baseline thickness used in these previous studies in our work to date. In particular, the effect of adding chevron-like sinusoidal spanwise crests and troughs along the trailing edge, especially their number and amplitude, is explored using LES and guided by the insights from an operator-based resolvent analysis. This method has been gaining traction since its extension to turbulent flows and such efforts are described in detail in Doshi et al 2021 and references therein. At its core the method solves an optimization problem, and hence modifications to the standard analysis have been pursued in the literature to tailor the results to specific objectives. In this effort, the focus is solely on the dynamics of the instability in the near vicinity of the wake of the splitter plate, hence a simplified representation of the configuration studied by Stack 2019 is used without sacrificing the fidelity of the dynamics of the flow. To this end, only the core stream, bypass stream and splitter plate are simulated with conditions matching that of the full configuration, and the SERN and deck surfaces are removed (Fig. 1).

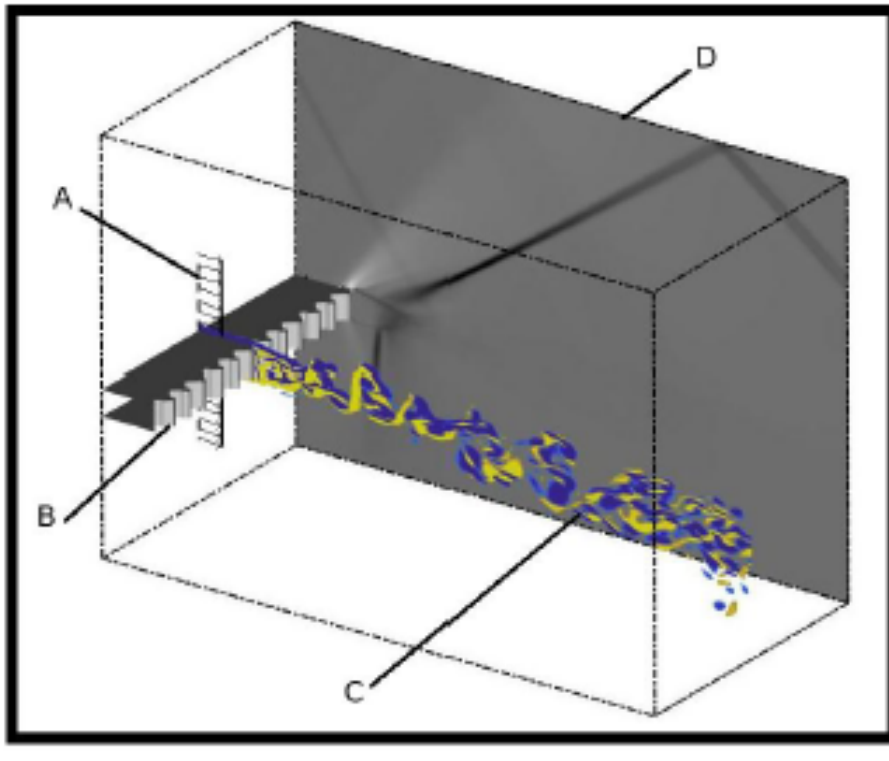

Figure 1. Schematic showing the main features of the simplified configuration used in this study. A) Incoming turbulent boundary layer B) Wavy trailing edge used for passive flow control C) Instantaneous vorticity plot D) Time-averaged numerical Schlieren showing the primary shock structure

The effects of the SPTE modifications are examined by simulating different control cases with varying spanwise wavenumbers and amplitudes of the crests. Additionally, an unmodified baseline case is also simulated to allow for a direct comparison. Details of the LES including numerical considerations are describe in Doshi et al. 2021a. Here we present the results of the resolvent analysis for the nominal case ($\beta = 0$) and the case with $\beta = 0.8$ which is used in the experiments.

The insights from the resolvent analysis are used to inform a passive flow control strategy based on modifying the SPTE. Although the resolvent is not informed by the intrinsic forcing, the instability corresponding to $St = 0.273$ and $\beta = 0$ is manifest in the unsteady flow; this indicates that the intrinsic forcing has some non-zero projection on the resolvent forcing mode corresponding to $\beta = 0$. Therefore, by modifying the shape of the SPTE, which has been observed to be the most sensitive region in the forcing mode plot it can be hypothesized that the same intrinsic forcing will now project on a trailing edge that is not straight but instead have sinusoidal variations built into it, and artificially alter the expected response. Figure 2 shows two forcing-response mode pairs in 3D, corresponding to $\beta = 0$ and $\beta = 0.8$ to further illustrate this point. The $\beta = 0$ forcing-response mode pair is nominally 2D and shows no spanwise variations by definition, while the $\beta = 0.8$ mode pair has 8 sinusoid wavelengths every 10 splitter plate thicknesses in the spanwise direction and travels in a direction oblique to the direction of the freestream.

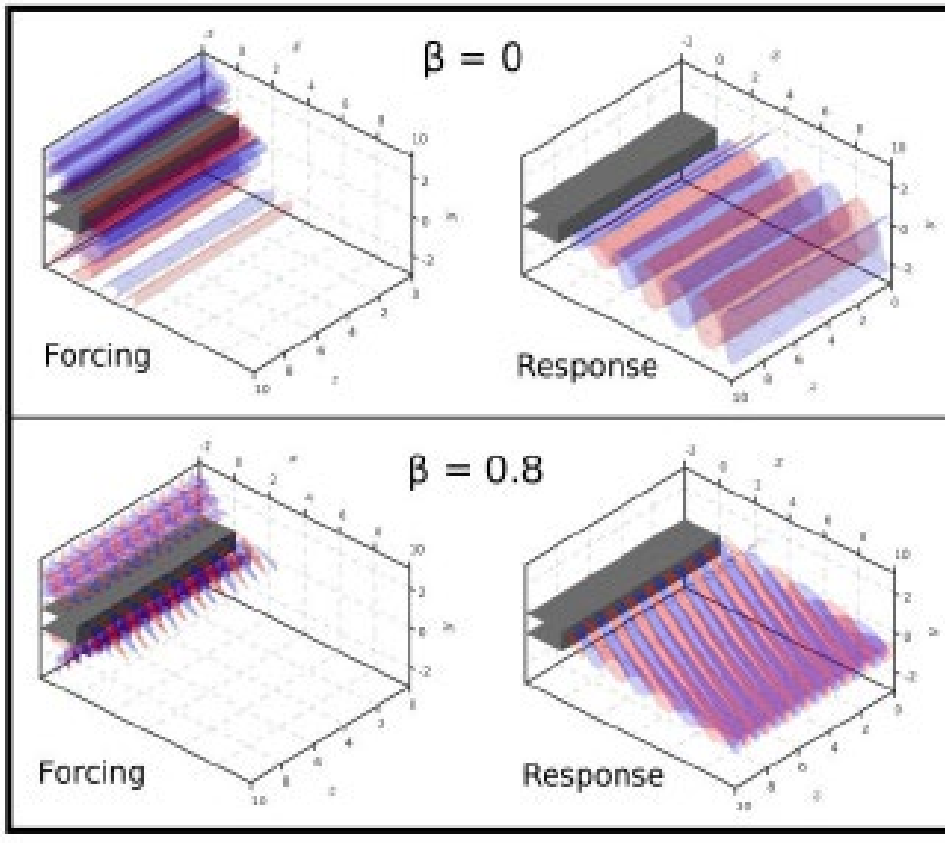

Figure 2. Resolvent forcing-response mode pairs visualized in 3D for $\beta = 0$ and $\beta = 0.8$. The lobes shown in these modes travel along and oblique to the direction of the freestream respectively. Other β mode pairs (not shown) have similar mode shape.

Intrinsic forcing in the unsteady flow has a non-zero component along the $\beta = 0$ forcing mode, and by changing the SPTE shape, specifically by creating 8 sinusoidal crests and troughs along the edge, that same intrinsic forcing projection can be expected to adopt the spanwise variations present in the $\beta = 0.8$ forcing mode, thus altering the overall modal characteristics by reducing the response for the $\beta = 0$ mode and increasing the response in the $\beta = 0.8$ mode. This understanding of the effect of the SPTE modifications however, neglects a key component of the non-zero β resolvent modes which are examined in Fig. 2. Since the $\beta = 0.8$ forcing-response pair have a spanwise component of motion which is absent in the trailing edge modifications, a second forcing-response pair with the same β traveling in the opposite direction needs to be superimposed onto the first pair so as to get a spanwise-stationary forcing-response mode pair that more accurately represents the spatially-stationary modified SPTE crests and troughs. This superimposed mode is visualized in Fig. 3 and has a checkerboard-like appearance.

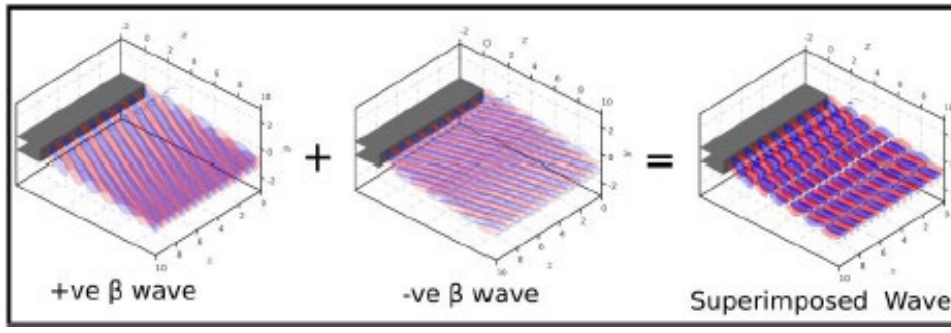

Figure 3. Three-dimensional resolvent mode plots of the normal component of velocity. Applying flow control through spanwise sinusoidal features along the trailing edge simultaneously excites two waves travelling obliquely with respect to the freestream, which superimpose to create a checkerboard-like interference pattern

In summary, the resolvent model provides sufficient insight into the characteristics of the flow to inform control action. Based on the resolvent model, although there is a point of diminishing return, increasing the wavenumber of the crests along the SPTE always improves the expected result in terms of control since the gain value always decreases with increasing β. The main parameters in the SPTE geometry for this study are the amplitude and wavenumber of the sinusoidal crest and trough features. To examine the effect of the variations in these parameters, four different SPTE profiles are simulated, and are summarized in Fig. 4. In addition to the four control cases (C1-C4), a baseline case is simulated consisting of a straight-edged splitter plate which represents the SPTE configuration that has been studied extensively before by Stack 2019, and used in the construction of the resolvent operator for the present work.

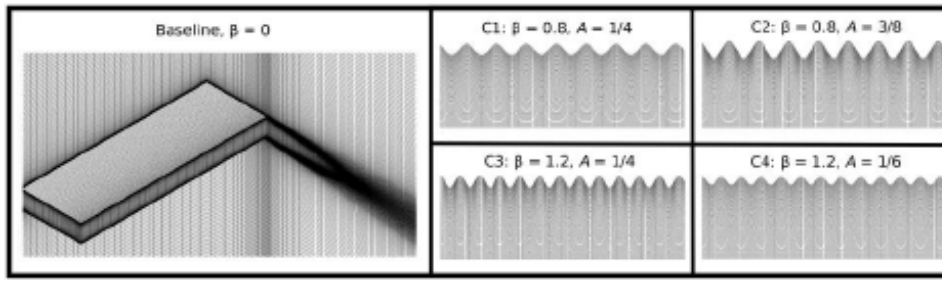

Figure 4. SPTE configurations used in this study, with every other point in the meshes shown for clarity. Here, β is the spanwise wavenumber while the symbol A denotes the amplitude.

The influence of the SPTE modifications on the flow is made visually apparent using the Q-criterion plot in Fig. 5. The baseline case shows a distinct presence of roller-like structures downstream of the SPTE, in accordance with the instability that has been the primary focus of this study.

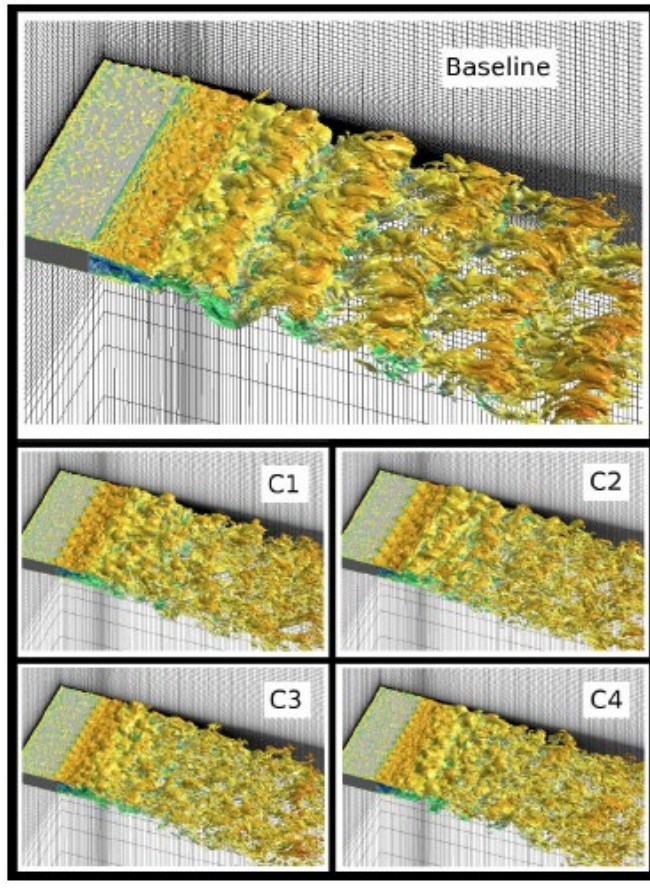

Figure 5. Isosurfaces of Q-criterion (isolevel of -0.4) colored by streamwise velocity for the cases in this study.

The rollers are also seen to be connected by rib structures, which are known to form in mixing layer flows (Hussain 1986). These roller structures can be discerned to a far lesser degree in all four control cases, and only up to a short distance from the SPTE. However, cases C1 and C4, which correspond to small-amplitude crests with $\beta = 0.8$ and $\beta = 1.2$ respectively, show a stronger signature of the roller structures than the large-amplitude cases C2 and C3. The crests act to induce streamwise vorticity in the flow due to their shape, and hinder the formation of the spanwise roller structures, while also enhancing the mixing between the two streams (Gist et al. 2020). Increasing β therefore, has a direct correlation with the degree of mixing between the two streams, as is apparent when comparing cases C1 and C2 with C3 and C4.

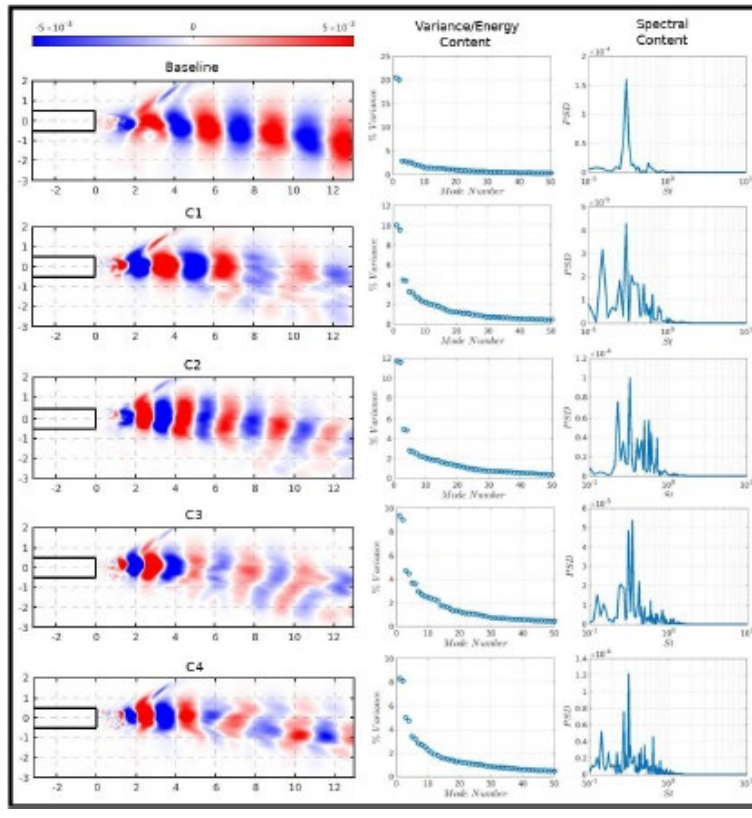

Figure 6. POD results obtained using 2D snapshots of the vertical component of velocity (v), extracted from a plane perpendicular to the spanwise direction at the center of the plate. Leading POD mode shapes (left) for all cases are similar between the first and second modes, due to the oscillatory nature of the flow. Their mode energies are also similar, as seen in the percentage variance plot (middle). Spectral content is computed using pressure time series data at a point probe in the flow, downstream of the SPTE (right).

To acquire additional insight into the dynamics of the cases, POD is performed using 200 evenly spaced two-dimensional snapshots of the flow with a non-dimensional time interval between them of 0.2 or approximately 2 microseconds.

The results of the analysis are shown in Fig. 6 along with the spectral data of the pressure time series collected at a point probe located approximately 13 and 7 splitter plate thicknesses downstream and above, respectively, of the SPTE, to examine the effects away from the immediate vicinity of the SPTE. The POD procedure solves for spatial functions that are optimal in the sense of capturing the greatest amount of variance in the data and to this end, the mean is subtracted from the snapshot data in the present computations to obtain modes that solely capture fluctuations about the mean. Data is therefore said to exhibit low-rank behavior, if a large percentage of the variance can be captured with a small number of POD modes, and high-rank if this is not true. The variable chosen for the POD was the

vertical component of velocity (v), to interpret the ranked modes according to the percentage of kinetic energy in the normal component of the fluctuations contained within them.

In all the cases examined, the leading POD modes have similar shape and occur in pairs as they represent traveling structures. Each mode in the pair is therefore phase shifted from the other by 90 degrees, and for simplicity only one mode from each pair is shown in Fig. 6. For the baseline case, nearly 40% of the fluctuation energy is captured by the leading pair of modes, and it has the least rank among all the cases in this study. The mode shape for this case shows zones of strong positive and negative correlation in the shear layer region, indicating the presence of the vortex instability. The power spectral density (PSD) data for this case also indicates a strong tonality in the flow, centered close to $St \approx 0.3$, which is close to the frequency predicted by the resolvent analysis. Cases C1 and C2, which correspond to the SPTE with $\beta = 0.8$, show an increased rank compared to the baseline, with the leading pair containing approximately 22% of the energy, and the correlation length of the mode shape being smaller than the baseline.

The spectral content for these two cases also indicates a more broadband distribution of frequencies compared to the baseline, although the signature of the baseline tone is still present to a substantially lesser degree in the PSD. The peak frequency corresponding to case C2 is slightly greater than that corresponding to C1, and the mode shapes of the two cases also reflect this fact. Case C2, which has a higher crest amplitude than C1, also shows a slightly lower rank than C1. The final two cases, C3 and C4, show the highest rank of all the cases, with the leading mode pair containing only 16% of the total energy in the flow. The correlation length is also smaller than both the $\beta = 0.8$ cases and the baseline case in addition to the fact that the PSD is also the most broadband. Case C3, with large $\beta = 1.2$ crest amplitude, appears to have a slightly lower rank than C4 similar to case C2 in comparison with C1. Therefore, the POD results conclusively indicate that increasing the number of crests per unit length along the SPTE increases the rank of the flow and decreases the correlation length of the modes while the PSD data shows that this has the effect of making the spectra more broadband. Increasing the amplitude of the crests for both $\beta = 0.8$ and $\beta = 1.2$ cases also showed a slight decrease in the rank of the flow compared to their small-amplitude counterparts.

The effect of the SPTE crests is examined in a more global sense by comparing two representative 3D DMD modes from the baseline case and case C2 in Fig. 7. The baseline case mode shows clear roller-like structures, with each pair of positive and negative rollers representing one vortex that forms over the splitter plate.

The rollers also appear to be contorting along the spanwise direction as they move downstream, due to the growth of a secondary instability. The DMD mode for case C2 shows a mixture of positive and negative correlation near the SPTE where mixing occurs between the two streams, and can be compared to the idealized superimposed resolvent mode. The rapid mixing action of the streamwise vortices

induced by the crests causes the behavior of the flow to rapidly become non-linear a short distance from the SPTE, beyond which the flow does not show a signature of the spanwise roller structures seen in the baseline case. As seen earlier, the rank of this flow is large and several modes of similar shape (not shown) are obtained from DMD for this case, as well as the other control cases in this study.

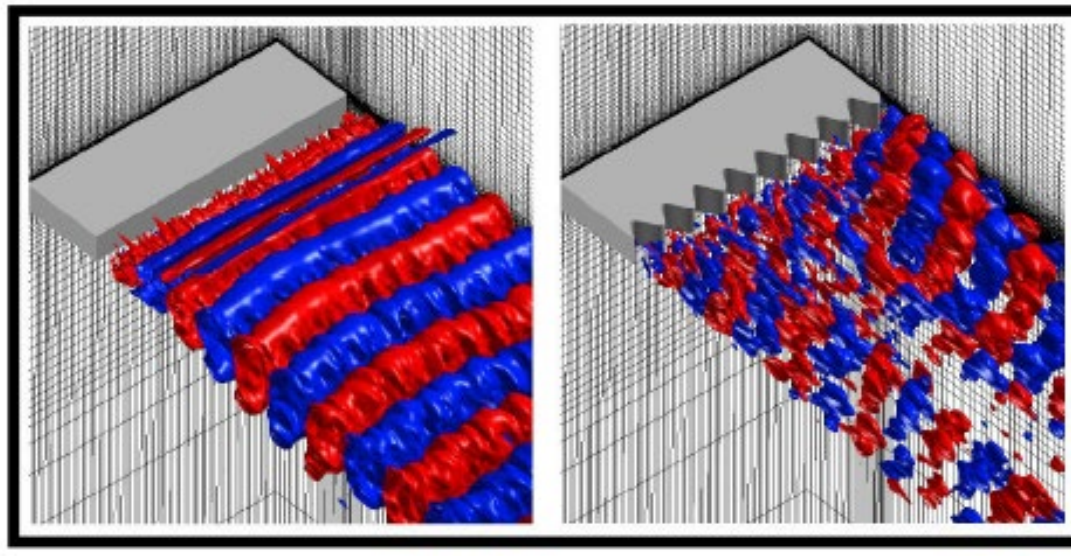

Figure 7. 3D DMD plots for a representative mode from the baseline case (left) and case C2 (right).

Experimental Passive Control of Full SERN Configuration

Experimental measurements are presented at this point in the final report which show the effects of passive control on the supersonic multi-stream rectangular nozzle. Preliminary experimental active control results which have been completed in the no-cost extension time period of the effort are presented later near the end of this final report. The configuration explored consists of a supersonic core stream (M = 1.6) and a sonic (M = 1) bypass stream which merge behind a splitter plate exiting into a Single Expansion Ramp Nozzle (SERN) and onto an aft-deck. Previous studies have deduced that the aft-deck geometry can alter the plume deflection and farfield acoustics, while the splitter plate has an influence on the shock train development and unsteady loading on the aft-deck due to the shedding instability behind the splitter plate. This campaign seeks to exploit the inherent receptivity of these regions by performing geometric modifications as a form of passive control. The study is broken down into two separate parts, the first being the aft-deck changes. Aft-decks explored vary parameters such as length, width, and chamfer from the nominal design to observe the influence of each on the flow.

Comparison to the nominal, half nominal, and no deck cases are in agreement with previous studies and show the plume deflection being a result of the shock train development. All deck modifications showed a slight upward deflection of the jet plume. The second effort of this study is the exploration of a sinusoidal spanwise wavenumber to the splitter plate trailing edge. Experimental design of the splitter plate is guided by Large Eddy Simulations (LES) discussed above. Particle Image Velocimetry and farfield acoustics are recorded for a wavenumber of 0.8 to match that of the LES. Both simulations and experiments show a reduction in the dominating tone. Results from both forms of passive control are compared with simulations.

Details of the Experimental Results

This study employs a modern nozzle design coupled with a variable cycle engine concept by Simmons 2009 displayed in Fig. 8. The design consists of a core stream, primary bypass and secondary bypass which exit into a Single Expansion Ramp Nozzle (SERN). Addition of the secondary bypass, or third stream, has been shown to provide benefits such as decreasing noise (Magstadt et al. 2015, Berry et al 2016 and Papamoschou and Debiasi 2001) improving operating efficiency (Simmons 2009), and can shield the aft-deck from thermal loading (Bruening and Chang 1999). Experimental configuration of this design is denoted the Multi-Aperture Rectangular SERN (MARS), displayed in Fig. 9. The nozzle design assumes a premixed core and primary bypass, referred to as the first stream in this paper and secondary bypass, which will be called the third stream, that are separated by a splitter plate. Design operating conditions maintain a first stream of Mach 1.6 and a third stream of Mach 1 of varying densities.

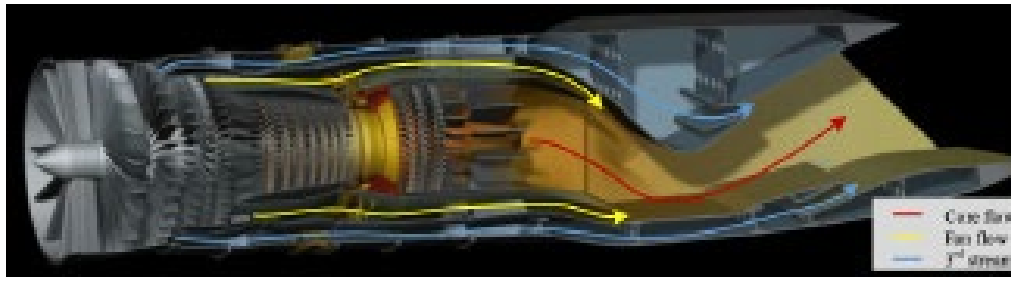

Figure 8. Variable Cycle Engine Studied by Simmons 2009.

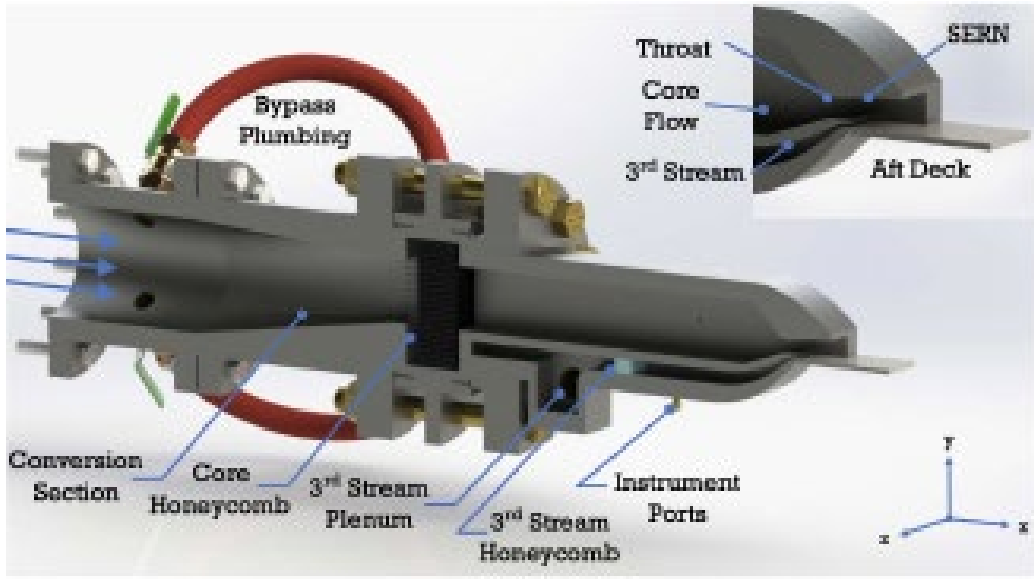

Figure 9. Rendering of the Experimental MARS at Syracuse University

Both streams merge behind the splitter plate before exiting into the SERN and over the aft-deck, which essentially mimics airframe integration. The turbulent flowfield consists of a complex shock-expansion wave system, shock-wave boundary layer interactions (SBLI), various boundary layers, and shear layers. Complexity of the flowfield is established by the SERN, splitter plate, and aft-deck. Aft-deck length has been explored in detail experimentally by Berry 2018, Berry et al 2017a, Berry et al 2017b and Magstadt 2017 and Magstadt and Glauser 2018, and using high fidelity Large Eddy Simulations (LES) by Stack & Gaitonde 2018 and Stack 2019 at the same flow conditions.

The aft deck has been shown experimentally to have effects on the shock train as well as the shape and deflection of the core jet plume Berry 2018. Through LES, Stack 2019 shows the plume deflection is connected to the shock train. Stack demonstrates that by adjusting the nozzle pressure ratio (NPR) and/or the deck length, the pressure field in the aft deck region is affected which subsequently affects the shock-train and resulting plume deflection. The previous studies have focused on the nominal deck length or those shorter than the nominal length with the exception of Gist et. al 2020 that discusses the effects of a deck extending past the nominal length.

Another advantageous component of the MARS is the third stream. The addition of the third stream to this design can shield the aft-deck from the shock downstream (Ruscher et al 2018) and provide a thermal barrier to the deck (Bruening and Chang 1999). However, the effectiveness of the third stream has been shown by the previously mentioned studies for this nozzle to be compromised by the shedding instability in the region of the splitter plate. Impact of this instability has been shown to have global detriment both acoustically and in terms of unsteady aft-deck loading. The dominating tone in the farfield has been linked to the vortex shedding instability of the splitter plate and occurs at half of the shedding frequency, 34 kHz for design operating conditions. The frequency of the shedding is controlled by the third stream speed (Magstadt 2017), that varies the characteristic frequency between 32-35kHz. The simulations described earlier provide clear evidence that an introduction of a non-zero spanwise wavenumber can alter the SPTE instability and reduce the dominant tone. Probes were used in simulations to investigate the effect of the wavenumber on the tone. A virtual probe was placed in the primary shock, the shear layer, the core stream and the deck

stream, which each showed the distinct high frequency tone for the nominal ($\beta = 0$) splitter plate case. In both non-zero beta cases, the presence of this tone was not as prominent or in some cases diminished completely. Effects of the introduced wavenumber on the flow physics are discussed earlier (reference Figures 5, 6 and 7), where the zero beta case shows coherent spanwise vortices. As the wavenumber increases, the number of lobed pairs of positive and negative streamwise vorticity increases. The introduction of this streamwise vorticity due to the SPTE wavenumber interrupts the formation of the spanwise vortices as can be seen in Figures 6 & 7. This leads to increased mixing between the layers and reduces the appearance of coherent structures shedding behind the splitter plate.

Demonstrated receptivity of the aft-deck and SPTE make these regions excellent candidates for flow control. Two forms of passive control are explored to the aforementioned nozzle components, both dealing with geometric modifications. The first is the modification of the aft-deck, more specifically, the length and chamfer of the trailing edge corners. In addition, geometric modifications to the SPTE are investigated. A wavenumber of $\beta = 0.8$ is used to match simulations and is compared to the nominal splitter plate case.

An alternative SPTE design is explored to match the simulations in described earlier. The smallest wavenumber, $\beta = 0.8$, non-dimensionalized by the SPTE thickness, has been deemed the most feasible from a machining aspect. Although a reduction in the SPTE thickness was shown to have a direct impact on reducing energies of turbulent instabilities Ruscher et al 2018 (most importantly the splitter plate shedding instability discussed prior), a constant thickness is followed for this study to directly focus on the impact of the introduced wavenumber. Fig. 10 displays the splitter plate that has been implemented in the MARS.

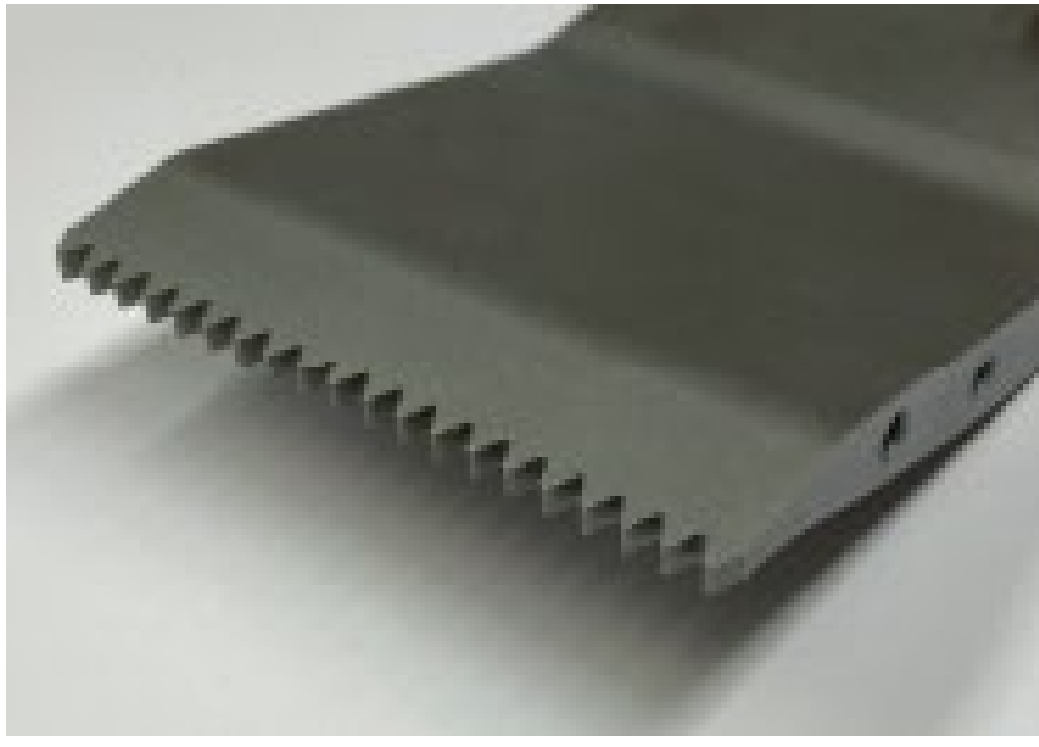

Figure 10. Machined splitter plate with wavenumber $\beta = 0.8$, used in experiments, selected based on LES results describe earlier.

A combination of Particle Image Velocimetry (PIV) and pressure measurements are used to analyze the response to the passive control methods proposed above. PIV and farfield microphones are sampled simultaneously with a minimally heated nozzle. All experiments took place in the anechoic chamber at Skytop Turbulence Laboratory at Syracuse University. Here we focus on the results specifically from the wavy plate shown in Figure 10 due to its connections to the simulations described earlier and compare to the nominal splitter plate case for the varying deck lengths. For more details on the effects of the deck plate geometries see Gist et al. 2021a and Kelly et al. 2021.

The results presented here compare the PIV measurements from the centerline streamwise plane along with far field pressure measurements of the no deck and nominal deck for each splitter plate with the first and third streams maintained at the design operating conditions of Mach 1.6 and Mach 1 respectively.

Far field measurements of the nominal aft-deck, shown in Fig. 11, shows a clear diminishment of the high frequency tone for the 120° microphone. This finding is consistent with simulation results of the same wavenumber described earlier.

The 34 kHz (St = 3.3) tone in the nominal plate case was found to be diminished in the case of the wavy splitter plate. As described in Gist et al. 2021a, the ½ deck and no deck cases exhibit similar results with the wavy splitter plate.

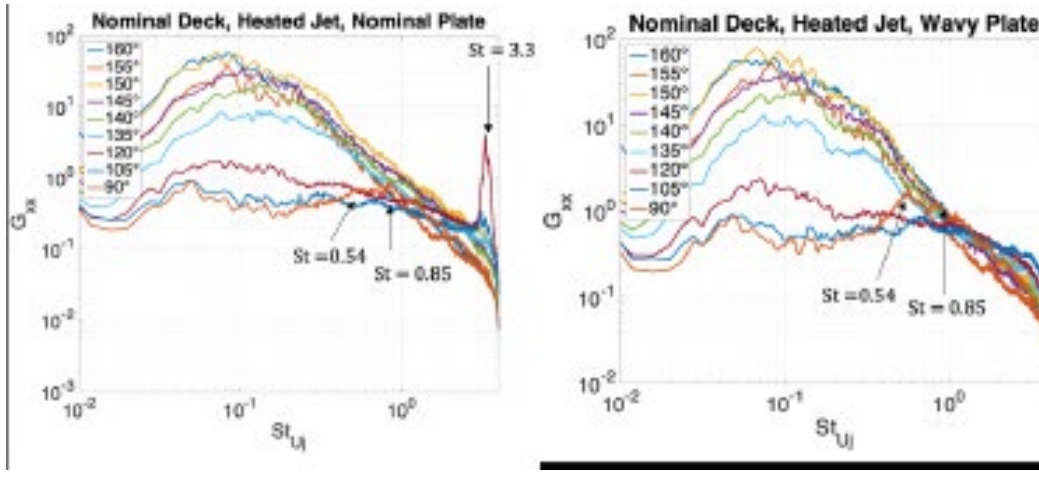

Figure 11. Single-sided autospectral density for the nominal aft-deck configurations with the nominal and wavy splitter plates.

PIV Measurements

PIV is utilized to measure the velocity field downstream of the jet nozzle. Seed particles illuminated by a pulsed laser sheet are recorded with a dual camera setup and allow for the acquisition of three components of velocity in a two-dimensional plane. The co-flow was seeded via a show fogger to ensure quality vectors in the entrainment regions. Plane locations are normalized by the nozzle hydraulic diameter of 44.5 mm. Velocity measurements are taken at several streamwise and cross stream locations. For each location at least three sets containing 400 images for each camera are taken and averaged for a minimum of 2400 images per plane. Figure 12 shows the streamwise and cross stream planes visualized over the test section. For more details see Gist et al 2022.

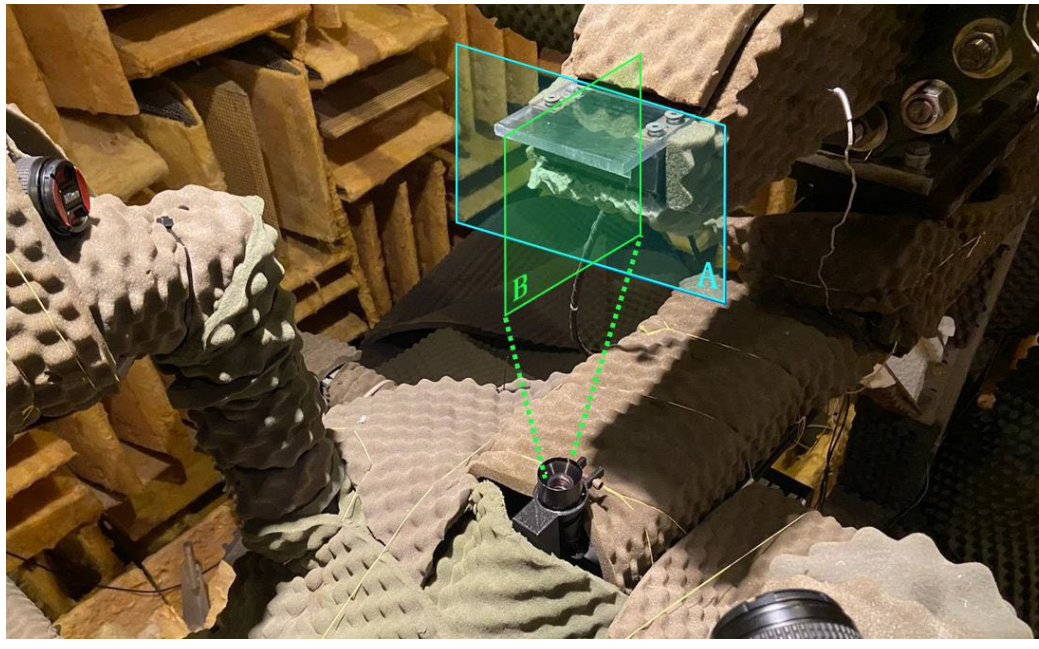

Figure 12. Plane orientations for cross stream (A) and streamwise (B) PIV.

PIV Statistics

PIV measurements have been carried out for the streamwise locations provided in Section III.A. Data presented in this study focuses on the centerline plane contour plots for the nominal, half and no deck configurations. Each experiment was carried out at design operating conditions of an exit velocity of Mach 1.6. The average velocity contour plots for the *u* and *v* components on the centerline plane for the nominal deck can be seen in Fig. 13. Evaluation of the u-component plots shows little differentiation between the shock cells in the averaged sense as the structure and speeds are similar. However, there is a modest uptick in the jet plume for the wavy splitter plate from 2 degrees to 3 degrees. To analyze this further, we can look at the mean *v*-component of velocity. As expected from the *u*-component contour, the *v*-component of velocity is a higher positive value downstream for the wavy SPTE, pulling the plume upward.

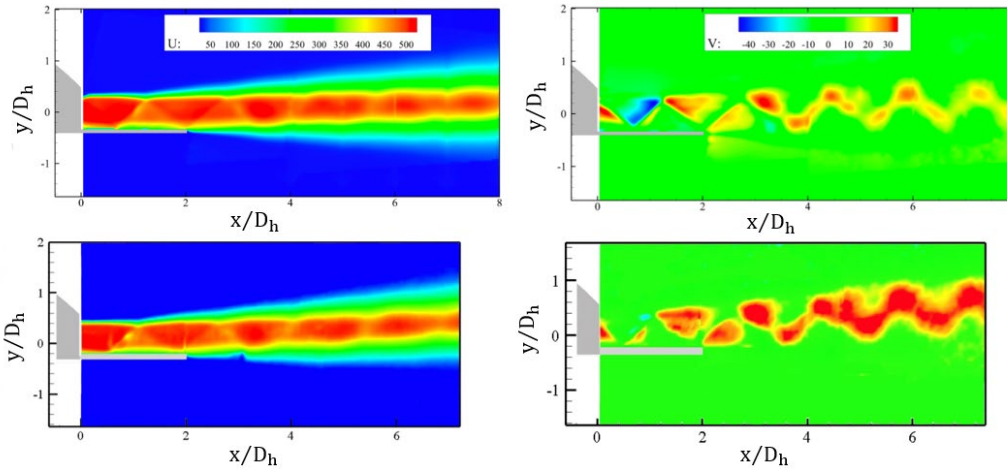

Figure 13. PIV measurements at centerline for nominal deck plate. Uncontrolled flow (top), Controlled flow (bottom), u-component (left), v-component (right).

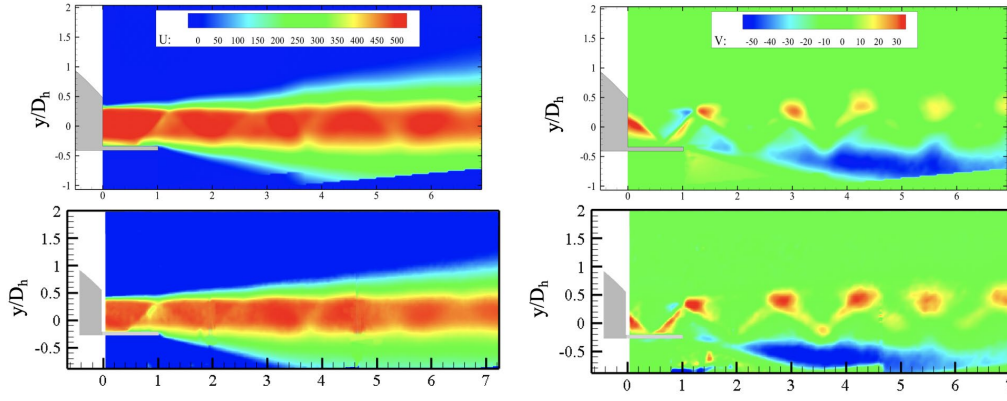

Figure 14. PIV measurements at centerline for half deck plate. Uncontrolled flow (top), Controlled flow (bottom), u-component (left), v-component (right).

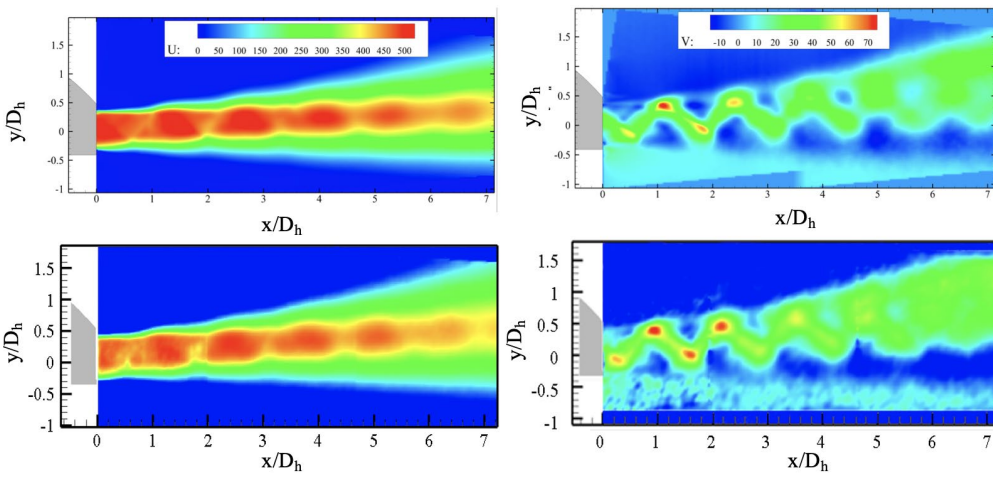

Figure 15. PIV measurements at centerline for no deck plate. Uncontrolled flow (top), Controlled flow (bottom), u-component (left), v-component (right).

In contrast to the nominal aft-deck results, the half deck and no deck configurations show little to no deviation between the nominal and wavy splitter plates. In the half deck case, results for both splitter plates show a strong downward deflection due to more mixing in the lower shear layer as the shock does not have time to reattach on the aft deck before the deck ends (Fig. 14). Shock cell locations, structure and average velocity for both contours do not show any significant difference. Mean *v*-velocity contours of this configuration are also in agreement, with the negative velocities in the lower shear layer which pull the jet plume downward. As with the half deck, the no deck case showed no significant change in the shear layer growth nor deflection angle of the jet plume (Fig. 15). However, there appears to be a slight increase in mixing at the nozzle exit for the wavy splitter case as the initial shock is less pronounced than in the nominal splitter case. The mean v-component speeds and shape of the shock cells are approximately the same for both no deck configurations.

LES of Full 3D SERN Geometry

The previous sections established the wavy SPTE as an effective passive means of controlling the vortex instability by creating spanwise phase variations in the vortex formation and introducing streamwise vorticity into the shear layer. This section examines the impact of introducing wavyness in the full SERN configuration using LES and data-driven techniques. See the Ph.D. thesis of Doshi at OSU 2023 for more details on these simulations. To accomplish this, a comparison between (1) a baseline configuration LES with the straight-edge SPTE and (2) a wavy configuration LES with a sinusoidal SPTE is performed; the details of the setup are presented below. Next, after a brief discussion of the salient differences between the downstream evolution of the two flows, the time-averaged and unsteady features are presented, followed by a summary of the LES results of the Full 3D SERN Geometry.

Simulation Setup

Figure 16 shows the SERN nozzle configurations simulated to study the effects of the wavy trailing edge. For the "wavy" configuration, the nondimensional SPTE wavenumber is $\beta \approx 0.31D$ where ‘D’ is the splitter plate thickness.

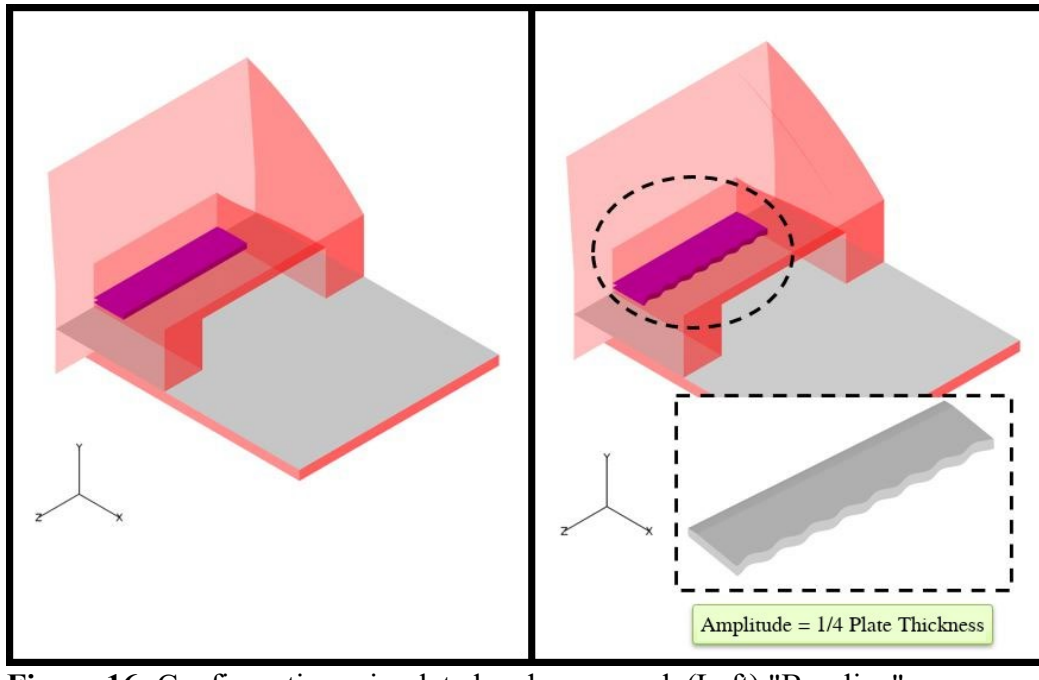

Figure 16: Configurations simulated and compared. (Left) "Baseline" configuration from Stack et al. 2018 (Right) "Wavy" configuration with a sinusoidal SPTE.

while the amplitude is the same. These parameters are selected based on the earlier results, that show even small spanwise wavenumbers to be effective in reducing the vortex instability. Furthermore, this creates a relatively mild geometric change over the baseline configuration at the most sensitive region of the shear layer, allowing for an effective study of the impact of the passive control method without introducing adverse secondary effects on the flowfield.

The simulations are performed following the setup in Stack et al. 2018. And correspond to a Reynolds number $\approx 1.81\times10^{6}$ and Mach number of 1. Time integration is performed using a second-order Beam and Warming method with a nondimensional time step size of $2\times10-4$, while spatial discretization uses the Roe scheme with third-order MUSCL reconstruction and van Leer's harmonic limiter for inviscid fluxes and a second-order central difference scheme for viscous fluxes. The domain is discretized using 1247 points in ξ , 463 points in η, and 305 in the ζ direction respectively, which constitute a grid of approximately 176 million points. Validation of the baseline setup and grid independence has been established by Stack et al. 2018 and is not repeated here for brevity. For the wavy configuration, the mesh around the SPTE is modified in a fashion similar to the shear layer configuration described earlier.

LES Results for Full Configuration

Figure 17 shows instantaneous snapshots on an axial (xy) plane passing through the spanwise center of the splitter plate. The shock structure and shear layers are visualized using contour plots of $u \cdot \nabla P$ (gray scale) and spanwise component of

vorticity ((∇×u) ・ k̂) respectively. In the baseline simulation, the periodic vortex formation and convection disturbs the oblique shock that forms immediately downstream of the SPTE; this unsteadiness is carried further downstream by the shock and has a global signature in the flowfield as shown by Stack et al. The wavy case on the other hand, shows a substantially weakened vortex formation — highlighted in the purple dash-dot box—and hence the oblique shock at the SPTE is more distinctly visible in the instantaneous snapshot. In addition to the unsteadiness, the separation bubbles at the foot of the shocks are also different in the two cases, with the baseline case showing a substantially smaller separation bubble than the wavy case on the SERN surface. This difference in separation bubble size leads to differences in the external shear layer structures(highlighted using the red dash-dot box) seen in the two cases, downstream of the nozzle exit.

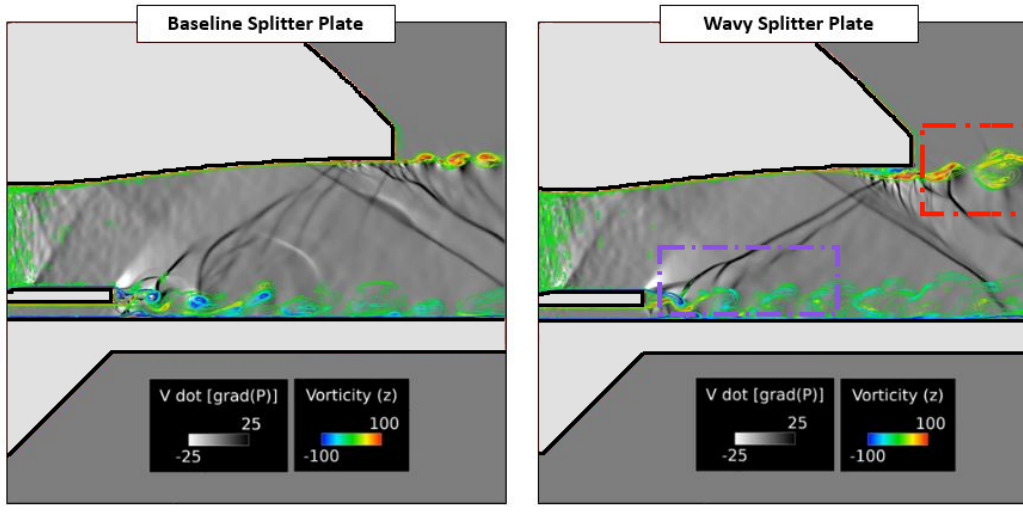

Figure 17: Unsteady snapshots of the two simulations in the symmetry plane. The purple dash-dot box in the wavy case shows the decreased strength of the vortical structures relative to the baseline case, while the red dash-dot box highlights the differences in external shear layer structures.

Further distinctions in the downstream evolution of the flow, including the reasons for the differences in the shock trains and SERN separation bubble size, can be understood by comparing various aspects of the time-averaged mean and unsteady features of the two cases, and are discussed in the following sections.

Time-averaged Flow

Since the SERN flowfield is statistically stationary, several insights can be obtained by comparing the time-averaged flowfields of the two configurations. To this end, instantaneous realizations of both configurations are collected and averaged using a minimum of 22,000 time steps, amounting to ≈ 44 non-dimensional time units or 11 flow-through times.

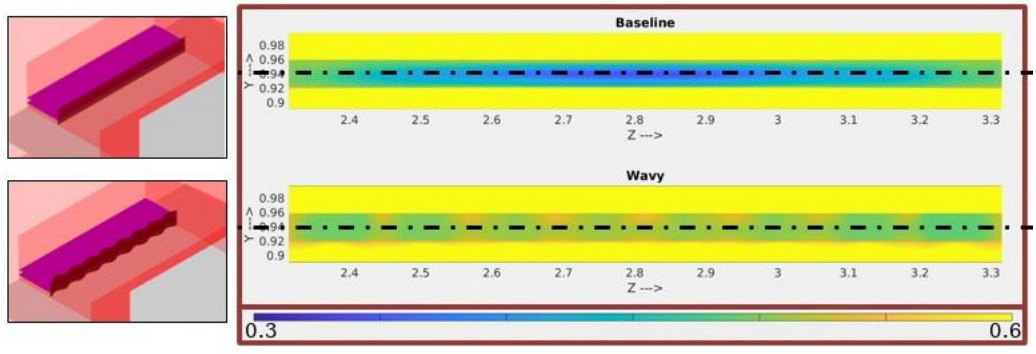

(a)

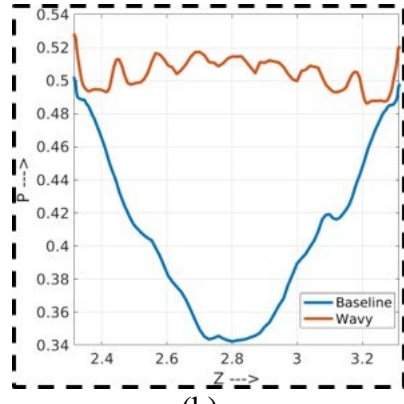

(b)

Figure 18: Time-averaged base pressure for the baseline and wavy cases. (Top) Contour plots on the base surfaces. The locations of these surfaces have been highlighted in brown in the left-side figures. (Bottom) A line plot created by plotting pressure along the dash-dot centerline in the contour plot.

Data from the resulting flowfields are compared in the following section.

SPTE Region

Starting with the SPTE region, differences in the strengths of the spanwise vortices formed in the two cases, as was shown qualitatively in Figure 17, manifest in differences in the time-averaged base (wake-side) surface pressure. This phenomenon is quantified in Figure 18, which shows contour and line plots of pressure on the base surface of the two SPTE configurations. The base pressure is observed to be substantially higher in the wavy case, especially at the spanwise center of the splitter plate, where the boundary layers on the side walls of the SERN geometry have the least influence on the vortex formation and shedding. This behavior is consistent with experimental observations of bluff body flows at incompressible speeds, where it has been shown that three-dimensionality in bluff body wakes tends to increase the base pressure due to reductions in vortex strength and consequent reductions in bluff body drag. Figure 18b further shows

that the mean base pressure in the wavy case is higher at the SPTE peaks and lower at the troughs.

The differences in base pressure manifest in differences in the sizes of the SPTE and deck separation bubbles and consequently the shock train evolution in the two flowfields, as illustrated in Figure 19. In this figure, the separation bubbles are visualized using isosurfaces of u−velocity ≈ 0 in Figure 19a and streamlines colored by u−velocity in Figure 19b and 19c. These plots show that due to the difference in base pressure, the size of the SPTE separation bubble is larger in the wavy case when compared to the baseline case, particularly at the trough regions.

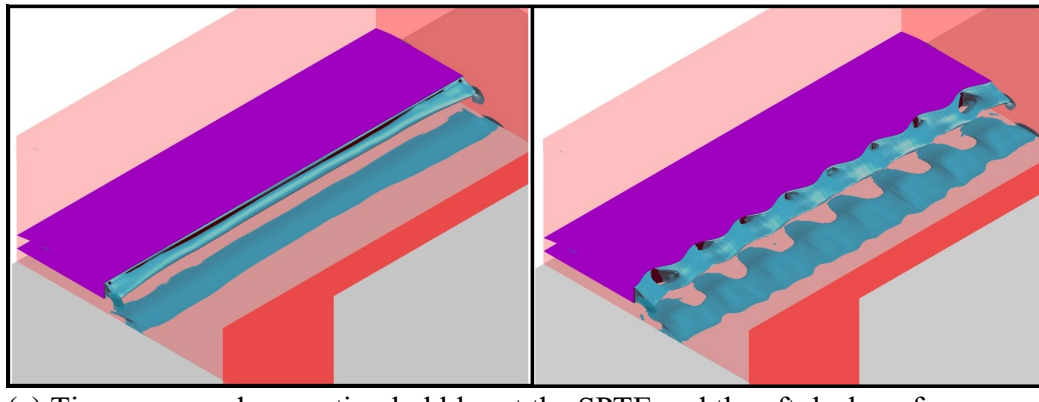

(a) Time-averaged separation bubbles at the SPTE and the aft deck surface, visualized using isosurfaces of u−velocity ≈ 0. (Left) Baseline configuration. (Right) Wavy configuration.

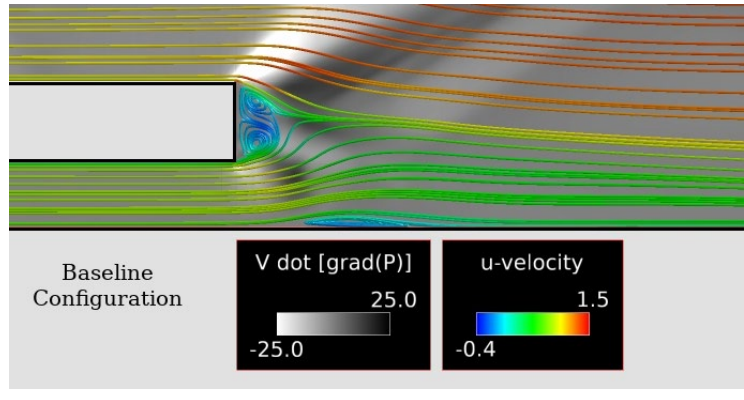

(b) Time-averaged streamlines colored by u − velocity and u ・∇P (gray scale) plotted in the central axial plane for the baseline configuration.

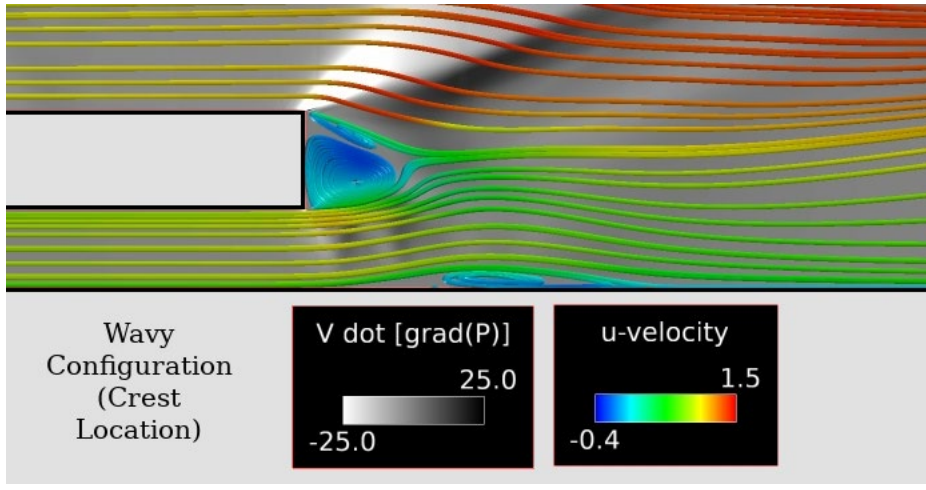

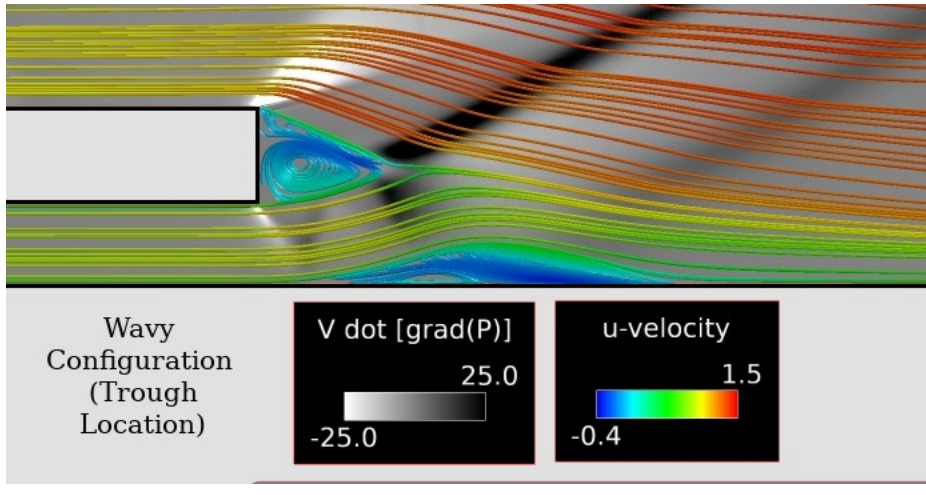

(c) Time-averaged streamlines colored by u−velocity and u ・∇P (gray scale) plotted in an axial plane close to the spanwise center for the wavy configuration. (Upper) Crest location. (Lower) Trough
location.

Figure 19: Near-SPTE separation bubbles and shock train

This can be attributed to the fact that the higher-than-baseline base pressure is less effective at turning the core and bypass streams on either side of the splitter plate towards each other, as visualized using the streamline plots in Figure 19b and 19c. The deck separation bubble and local shock structure are also remarkably different in the two configurations. Figure 19a shows that while the baseline deck bubble is nearly homogeneous in the spanwise direction, the wavy case shows a spanwise wavy separation bubble, with the streamwise extent of the bubble being greater at the SPTE trough locations than the peaks. This difference can be explained by examining the shock structure at the SPTE region as visualized in Figure 19b and 19c. The deck separation bubble forms due to the adverse pressure gradient imposed by the lower SPTE shock structure on the deck boundary layer. Due to

the geometry of the wavy SPTE, this shock structure begins upstream of the baseline SPTE at the trough locations, whereas the opposite is true of the peak locations; thus, the deck separation starts earlier at the troughs than the peaks, and a wavy separation bubble is formed on the deck surface. The spanwise wavenumber of the wavy bubble is equal to the wavenumber of the SPTE. Turning of the core stream into the deck stream occurs through the upper SPTE expansion wave and oblique shock system. In the baseline case (Figure 19b), this system is nearly invariant in the spanwise direction, except at the regions close to the sidewalls due to three-dimensional effects. For the wavy case however, the oblique shock shows different behavior at the peaks and troughs. Figure 19c(upper) shows that the oblique shock above the SPTE is thicker along the streamwise direction at the peak regions, extending from the SPTE to the location where the core and deck streams meet. On the other hand, at trough locations (Figure 19c(lower)), the oblique shock is sharper and exists downstream of the SPTE, thus imparting a spanwise waviness to the complete oblique shock structure; this point is illustrated later, in the context of Figure 21.

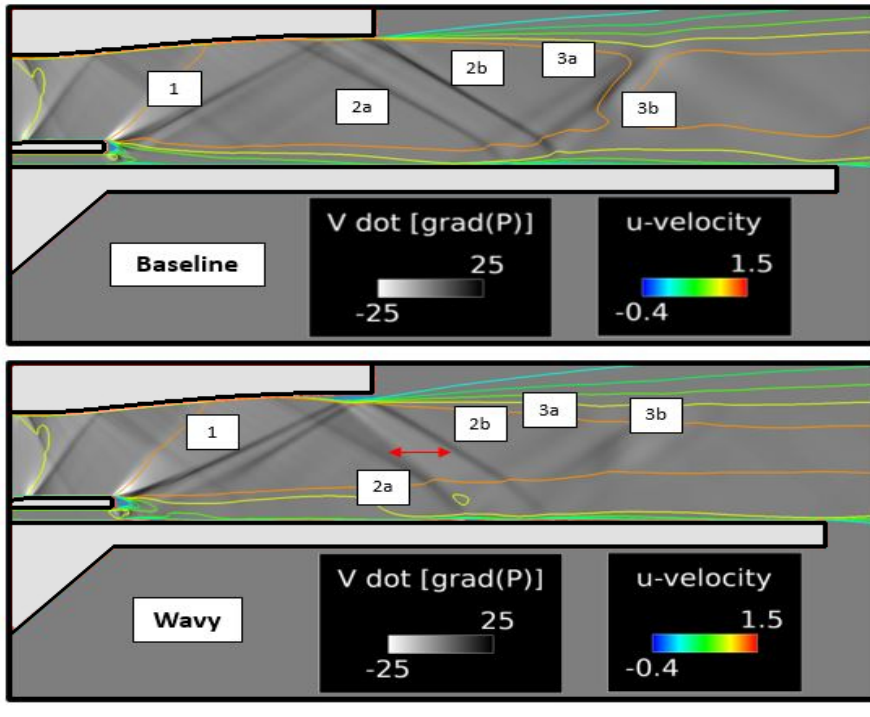

Figure 20: Contour plots of u−velocity (lines) and u ・∇P (filled, gray scale) for the two configurations.

Mean Shock Structure

The mean shock structure on the central axial plane of both configurations is highlighted in Figure 20, where individual shock components have been labelled according to the nomenclature used by Stack et al. 2018. Oblique shock '1' is produced by the interaction of the core and bypass streams, and reflects off the SERN surface as '2a'. A relatively weak separation shock — which meets '1' at the SERN separation bubble — is also produced by the deck separation bubble; this shock is stronger in the wavy configuration than the baseline configuration.

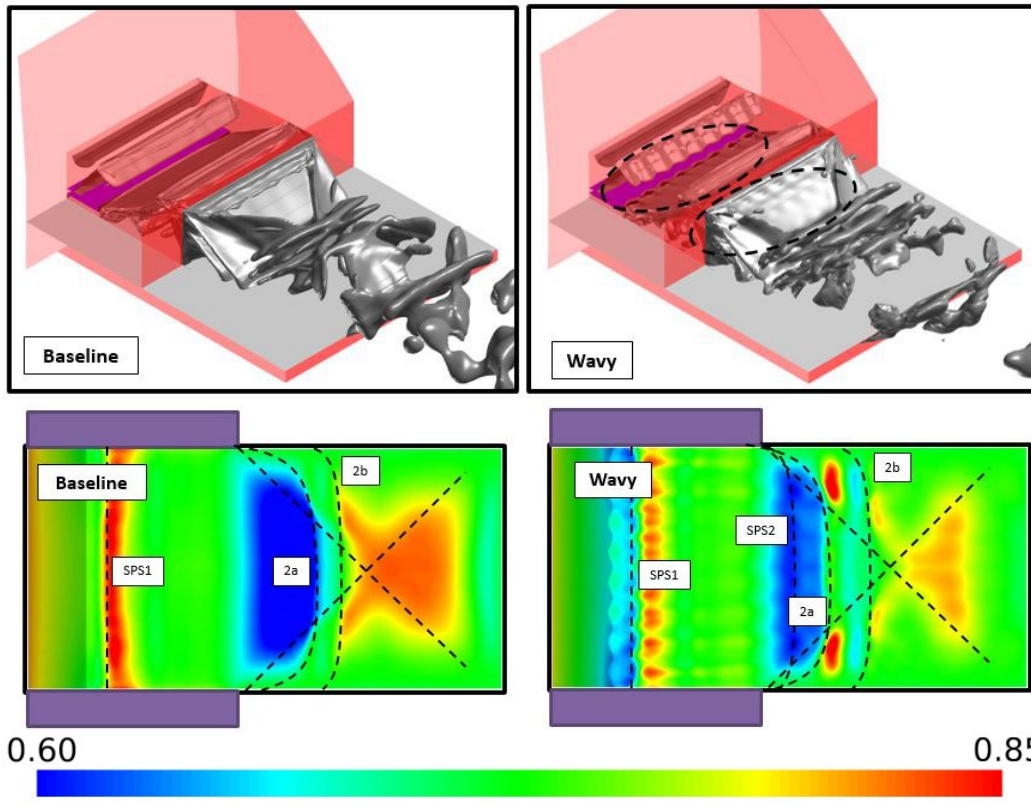

Figure 21: (Top) Shock structure for both configurations, visualized using isosurfaces of u ・∇P (isolevel of 0.3) (Bottom) Pressure contour plots emphasizing the gradients imposed by the shock structure on the deck surface. Shocks have been indicated using dotted black lines, while the splitter plate surface and side wall cross-sections have been shown using faded black and purple regions respectively.

Differences in the strengths of the impinging shocks on the SERN surface create differences in the SERN separation bubble size, and further increase the separation between '2a' and the oblique shock created by the overexpanded core stream exiting into the environment (labelled '2b'). This feature has been highlighted in Figure 21 using the horizontal double-sided red arrow.

To the study the impact of the mean shock structure on the deck boundary layers,

Figure 21 shows the mean structure in the two configurations (Figure 21(top)) and the deck surface pressure distribution (Figure 21(bottom)). The regions highlighted with black dotted lines in the top figure indicate the waviness in the oblique shock system alluded to earlier. Meanwhile, the dotted lines in the bottom figure delineate the complete oblique shock system on top of the deck. Pressure gradients on the deck surface (Figure 21(bottom)) can be attributed to the shock system and the presence of separation bubbles. Beginning from the SPTE and moving downstream, both wavy and baseline configurations show a compression due to the separation shock (SPS1) created by the deck separation bubble. Unlike the baseline case however, the wavy case shows some expansion immediately before 'SPS1', due to the fact that the SPTE separation bubbles are different in both cases and create different shock systems within the bypass stream (see Figure 19). Next, the flow encounters a decrease in pressure as the jet exits out of the nozzle, with the drop in pressure being greater in the baseline case than the wavy case, followed by a second separation shock (SPS2) created by another separation bubble. Due to the overexpanded nature of the core stream, two spanwise oblique shocks are also created in both baseline and wavy configurations. The remaining pressure gradients are thus explained by the interaction of shocks '2a', '2b' and the spanwise oblique shocks with the deck boundary layer.

Mean TKE

To visualize zones in the flow where turbulent fluctuations are strongest, Figure 22 presents the time-averaged turbulent kinetic energy (TKE) of the two configurations in streamwise and spanwise planes. The planes selected to create the plots have been shown at the top of the figure using a schematic; the streamwise (xy) plane is spanwise-centered while the spanwise (xz) plane is centered about the thickness of the splitter plate.

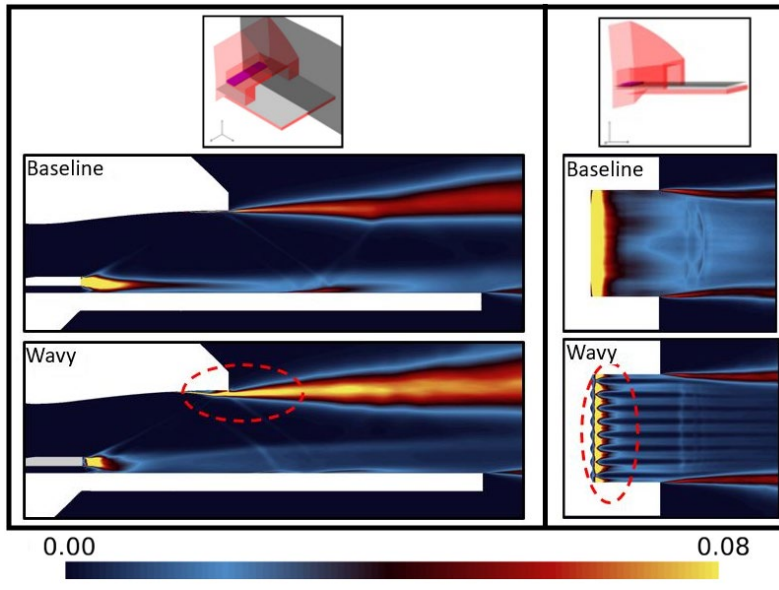

Figure 22: TKE plots of the two configurations in (left) axial and (right) spanwise planes.

Changes in TKE caused by the wavy SPTE have been highlighted using the red dotted ovals. In both baseline and wavy configurations, the TKE is large in the wake of the SPTE region, where the vortices initially roll-up and start to convect downstream. However, the magnitude and spatial extent of this high TKE region is substantially larger in the baseline simulation, as seen in the spanwise TKE plots. This further suggests that the strong fluctuations associated with the formation of coherent spanwise vortices is greatly diminished in the wavy SPTE simulation. Additionally, the spanwise TKE plot for the wavy SPTE shows the TKE to have a larger spatial extent at the peaks than the troughs, indicating that the wavy plate may create vortex dislocations at the troughs like the small β simulation described earlier.

The impact of the oblique shock '1' and deck separation shock 'SPS1' on the SERN separation bubble, seen earlier in the context of Figures 17 and 20, is also manifest in the streamwise TKE plots. The wavy configuration shows a substantially larger TKE production at the SERN bubble, extending downstream into the upper shear layer formed by the core stream as it exits the nozzle. This behavior is consistent with the larger vortical structures seen around the SERN separation bubble in Figure 17, and is a consequence of the fact that the Kelvin-Helmholtz instability within the separated shear layer grows more than in the baseline case. The unsteadiness created by the instability is also manifest in the SPOD results, as described below.

Unsteady Flow

The spectral POD technique is applied in the same streamwise and spanwise planes shown in Figure 22, to compute the energy spectra and dominant mode shapes, and the results are the presented in Figure 23. For each of the computations, 2000 evenly-spaced snapshots of v−velocity are used with a time-interval of 100 nondimensional time units. The snapshot matrix is windowed into 7 equal bins with a 50% overlap between them, and a Hamming windowing function is employed to compute the spectra. Furthermore, to assess the rank nature of the flows at various frequencies, only the leading two mode energies are plotted for clarity. The mode shapes shown in Figure 23 are the leading mode shapes at the frequencies color-coded with the circles in the spectral energy plots.

In the streamwise plane (Figure 23a), the baseline simulation shows the familiar lowrank large peak at ~ 31.2kHz, which corresponds to the vortex instability of interest in this dissertation. The instability is coherent up to a large streamwise distance, and also has a signature along the oblique shock '1' and in the farfield. On the other hand, in the wavy simulation, two low-rank spectral peaks are seen at ~ 2.1kHz and ~ 35.4kHz respectively. The 35.4kHz peak corresponds to the vortex instability, but is coherent up to a smaller streamwise distance than the baseline simulation and is 2.5 times weaker. Meanwhile, the 2.1kHz peak is associated with the SERN separation bubble, shocks '2a' and '2b', and the upper shear layer created by the core stream upon exiting the nozzle. This indicates therefore, that while the wavy splitter plate diminishes the vortex instability at the SPTE, it also

enhances a lower frequency unsteadiness at the SERN separation bubble. These observations are further corroborated by examining the SPOD results in the spanwise plane (Figure 23b). In the baseline simulation, two low-rank peaks with a small frequency separation between them are obtained. While the 31.2kHz peak is associated with the vortex instability phenomenon that has been described thus far, the 33.7kHz peak can be understood to be a result of the vortex instability interacting with the boundary layers on the side walls of the nozzle, which create spanwise dislocations on the SPTE and form vortices at a slightly higher frequency. Therefore, while the side walls have a strong effect on the base pressure distribution (Figure 18b), they also have a slight effect on the frequency of vortex formation in the baseline simulation. In the wavy simulation, two peaks are observed at frequencies of 2.5kHz and 35kHz respectively. The 35kHz frequency, which is associated with vortex formation near the SPTE, is not low-rank, but the mode shape of the leading SPOD mode shows spanwise dislocations and cells similar to the small β simulation described earlier. On the other hand, the 2.5kHz frequency is low-rank, and shows large magnitudes at the side shear layers created by the core stream exiting the nozzle, as well as around the shocks '2a' and '2b' which intersect the spanwise plane where the snapshots were taken.

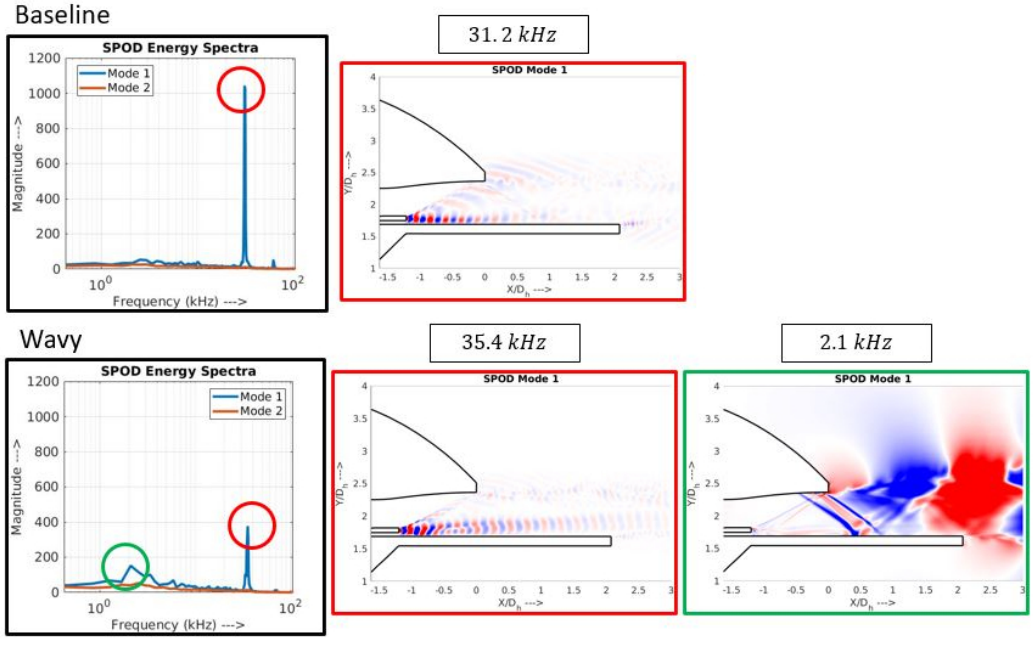

(a)

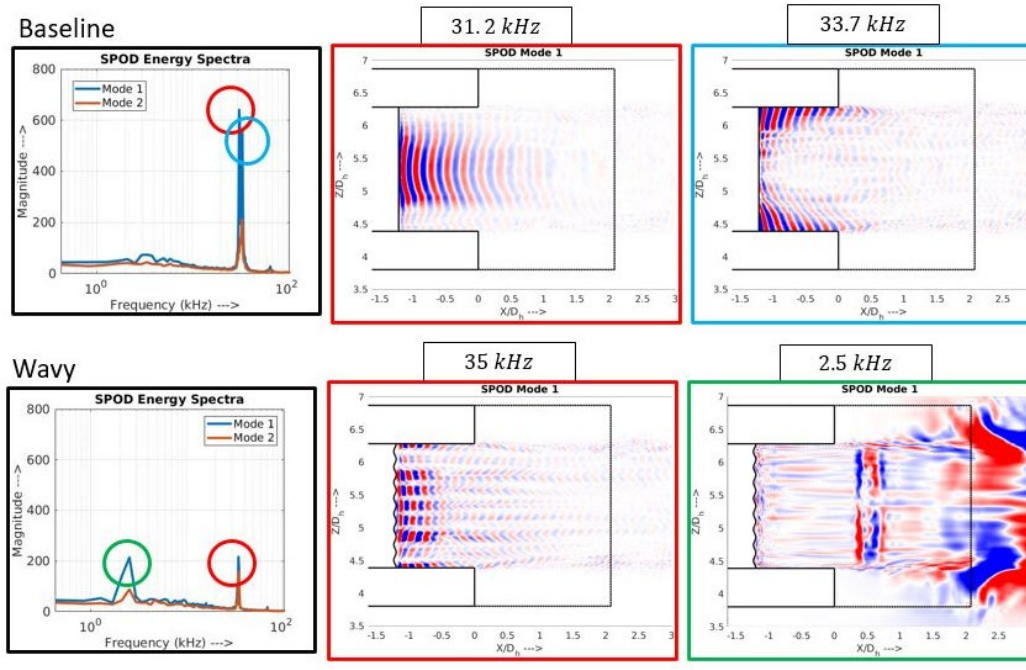

(b)

Figure 23: SPOD results from v−velocity data obtained from (a) streamwise and (b) spanwise planes. The locations of the planes are identical to those in Figure 22.

Summary of LES Simulations in Full 3D SERN Configuration

LES and data-driven modal analysis was used to examine the impact of incorporating a wavy SPTE in the nozzle configuration of interest, with the purpose of controlling the vortex instability identified in previous studies (Stack et al 2018). To this end, the simulation setup from Stack et al. 2018 was modified to include a wavy splitter plate, to compare with a baseline (straight-edge SPTE) case. The key results from the LES of the full 3D SERN configuration can be summarized as follows:

1. Despite the small spanwise wavenumber and amplitude used in the wavy simulation (β = 0.31D, Amplitude = 1/4D), the wavy splitter plate substantially reduced the formation of coherent spanwise vortices, with the SPOD mode energy reducing by a factor of 2.5 in the streamwise plane. Additionally, the frequency of the mode shifted to a slightly higher frequency (31.2kHz −→∼35kHz), while its streamwise correlation length reduced.
2. Due to the reduction in the formation of coherent spanwise vortices near the SPTE, the wavy simulation exhibits a substantial increase in mean base pressure, which consequently increases the SPTE separation bubble size and alters the local shock system around it. This effect is especially profound on the bypass stream side, leading to the formation of a large

wavy deck separation bubble that in turn creates a strong wavy separation shock.

3. The changes to the local shock system introduced by the wavy splitter plate lead to a larger SERN separation bubble, as well as accentuating the Kelvin-Helmholtz instability within the separated shear layer. This creates an additional, low-frequency unsteadiness in the flow of ~ 2.1−2.5kHz.

Preliminary Experimental Active Control Results of Full SERN Configuration

A framework for active control of the SERN flow is considered for analysis and comparison to the baseline flow inspired by the success of the passive control discussed in the previous two sections. The control mechanism involves the introduction of a microjet array to blow sonic air into the region where the two streams meet. Steady blowing of the jet array seeks to alleviate the unsteadiness found to be associated with the complex instability that results from the two streams interacting, perturbing the shock train and propagating throughout the flowfield. Far-field pressure as well as Schlieren imaging, are used to fully quantify the baseline as well as the controlled flow for several actuation configurations. See Kelly et al 2023 for more details.

A CAD model of the active control design mounted on the jet nozzle can be seen in Figure 24. The high pressure line is fed through a premium solenoid on/off valve. This valve is a drop assisted 24V DC valve, when no current is supplied to the valve, it's default state is closed. Providing a current to the valve causes it to open. Adjustment of the duty cycle of the voltage signal applied to the solenoid valve will allow for this unsteady actuation in future experiments. Following the high pressure air at it moves through the bypass line and solenoid valve, it is then directed into an aluminum plenum chamber. This chamber, the rectangular box below the deck plate in Figure 24, utilizes the existing bolts used to attach the aft deck plate. Within the plenum chamber the flow passes though a converging section towards a slot across the deck plate allowing for choked, sonic conditions emanating from the holes that lie within that slot. Also, within the plenum chamber is a pressure sensor used to obtain instantaneous measurement of the NPR for the jets in supersonic crossflow (JISC). For the holes within the deck plate there are 19 2*mm* diameter holes. The locations of the holes correspond to the trophs of the wavy splitter plate used in the passive studies, taking advantage of the resolvent analysis already performed that determined the spanwise wavenumber. The holes are located 4.13*mm* away from the deckplate, and thus the splitter plate trailing edge (SPTE), this distance corresponds to the distance between two successive peaks on the wavy splitter plate. These hole locations are the closest to the SPTE given practical machining constraints.

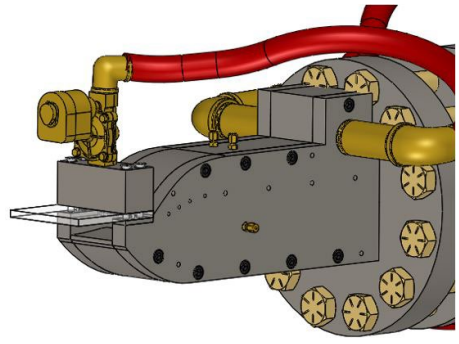

Figure 24: CAD model of active control mechanism mounted on the jet nozzle.

Pressure probes are dispersed in the near-field and far-field of the domain to capture time-resolved information at a rate of 100 kHz. Kulite pressure transducers are used for unsteady surface pressure measurements along the aft-deck. The deck begins at the trailing edge of the splitter plate and extends beyond the nozzle exit to 2 hydraulic diameters (= 44.5 mm) downstream. Measurements are taken just aft of the SPTE across the span to identify potential differences in the peaks and troughs Acoustic microphones in the far-field acquire data simultaneously with the near-field transducers. Nine G.R.A.S. microphones are positioned 85 hydraulic diameters downstream in-plane with the nozzle. The anechoic chamber facility as well as a schematic of the microphone array can be seen in Figure 25. The pressure measurements obtained are used to estimate power spectral density (PSD).

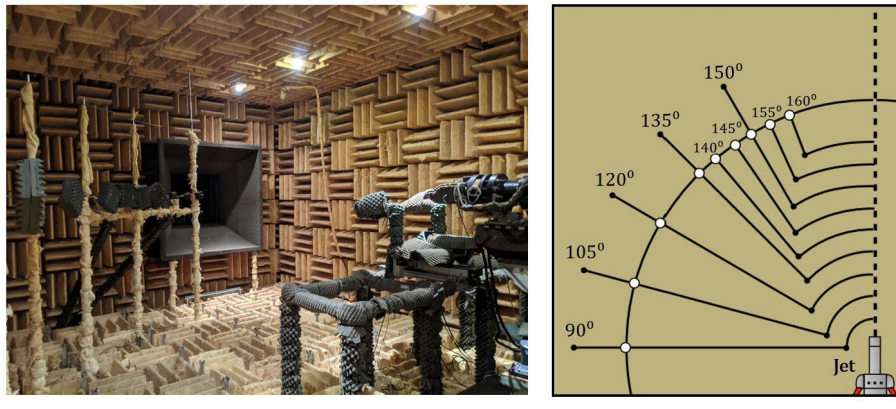

Figure 25: Anechoic chamber (left) and location of far-field mic array (right).

In order to measure variations in the index of refraction of the flow field and visualize the density gradients allowing for analysis of shock locations, a modified z-type schlieren system is set up within the anechoic chamber. The system is comprised of parabolic mirrors, a high powered lighting element and camera to acquire the data. The schlieren setup with labeled components can be seen in Figure 26. For each of the tests the camera recorded video at 60 Hz with a viewing window of roughly 2.5 hydraulic diameters. 300 frames over a 5 second acquisition period when the jet achieves steady state conditions are overlaid and averaged in order to obtained mean shock locations. The full schlieren setup was then traversed downstream to two locations in the streamwise direction 50mm and 100mm downstream. Experiments were repeated at these alternate viewing windows and the final averaged images were stitched together in order to obtain the density field for the entire jet plume out 4 hydraulic diameters from the nozzle exit.

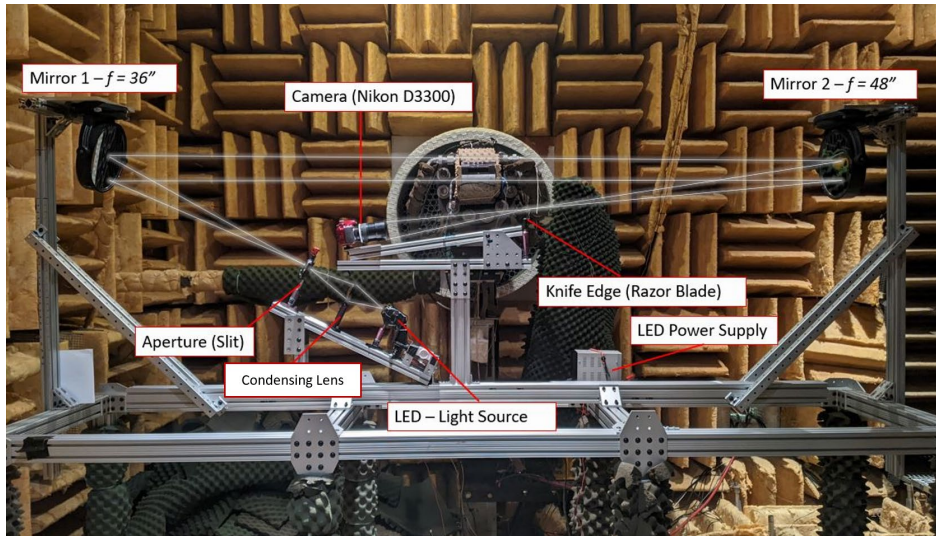

Figure 26: Modified Z-type schlieren setup used in experiments.

A parametric study was conducted to understand the effect of steady blowing on the mean shock structures. All tested were conducted at the jets nominal operating conditions of: NTR 1.0; NPR1 4.25 (M1 = 1.23); NPR3 1.89 (M3 = 1.0) and the Mach number of the Micro jets of 1.0.

Several actuation configurations were tested in addition to the baseline un-actuated flow. The slot in the active plenum chamber acts as the maximum actuation area. The 4 actuation cases, herein referred to as cases B-E, look into the effect of changing the angle of the holes (C) as well as the diameter of the holes (D). Finally a maximum momentum case (E) is tested corresponding to actuation of the entire slot. Table 1 provides an overview of the different test cases with their corresponding coefficients of momentum. The coefficient of momentum specifies the ratio of the mass flux between the actuator and bulk flow. For each of the test

cases far-field acoustic measurements as well as averaged schlieren videos were recorded.

Test Cases		
A	Baseline Flow (no actuation)	$C_\mu = 0.0000$
B	19 2mm diameter holes	$C_\mu = 0.0084$
C	19 2mm diameter holes angled at 45°	$C_\mu = 0.0084$
D	19 3mm diameter holes	$C_\mu = 0.0190$
E	Full open slot	$C_\mu = 0.0394$

Table 1: Preliminary Experimental Parameters: Actuator Conditions

Far Field Spectra

The initial active control campaign goal is to gain insight into the effect that steady blowing has on the mean shock structure as well as far field acoustic spectra. The spectra of the baseline flow can be seen in Figure 27, where the SPL is plotted against the log of St to get a sense for the noise distribution across the various frequencies within the flow. The different microphone locations are shown with the colored lines. This plot shows the distinct signature of the jet configuration found in previous studies: the dominant high frequency peak existing at St = 3.3. This peak is most prominent in the 120 degree microphone, but it is present at all spatial locations. Furthermore there exists another, smaller, high frequency peak at St = 1.495. The existence and intensity of the dominant peak marks the parameter of interest for flow control, i.e. *How can steady actuation effect this frequency peak?*

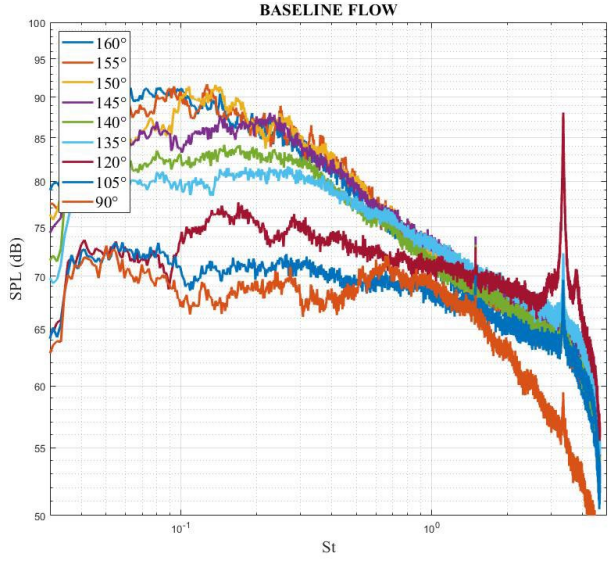

Figure 27: SPL vs St for baseline un-actuated flow (Case A)

For all actuation cases both the amplitude (SPL) and location (St) of the dominant frequency tone were affected. Table 2 shows the SPL and St of the peak for all of the test cases. For all cases with actuation the frequency of the tone was lowered. The SPL of the tone was amplified for cases B and D, while cases C and E lowered the noise level. Cases C and D display the largest effect on the dominant tone in terms of diminishment and amplification respectively. Figure 28 shows the far-field spectra for Cases C and D. The effect on the high frequency peak can be seen clearly. Observing the plot for Case C, it can be seen that the second, smaller, high frequency peak previously at St = 1.495 in the baseline flow has been shifted down to St = 0.5318. This small peak is relatively unaffected in Case D. Shifting focus back to the dominant peak, Case C showed a reduction of roughly 8 dB compared to the baseline flow whereas Case D showed an increase by 8 dB. Furthermore Case D saw a "thinning" of the frequency peak indicating possible organization of the flowfield, and the largest reduction in the frequency tone from St = 3.346 down to St = 2.952. The smallest change to the frequency occurred in Case C where the tone was present at St = 3.282.

SPL and St of High Frequency Peak		
Test Case	St	SPL [dB]
A	3.346	88.1
B	3.029	90.7
C	3.282	80.7
D	2.952	96.2
E	3.074	87.5

Table 2: Details of Dominant Frequency Tone

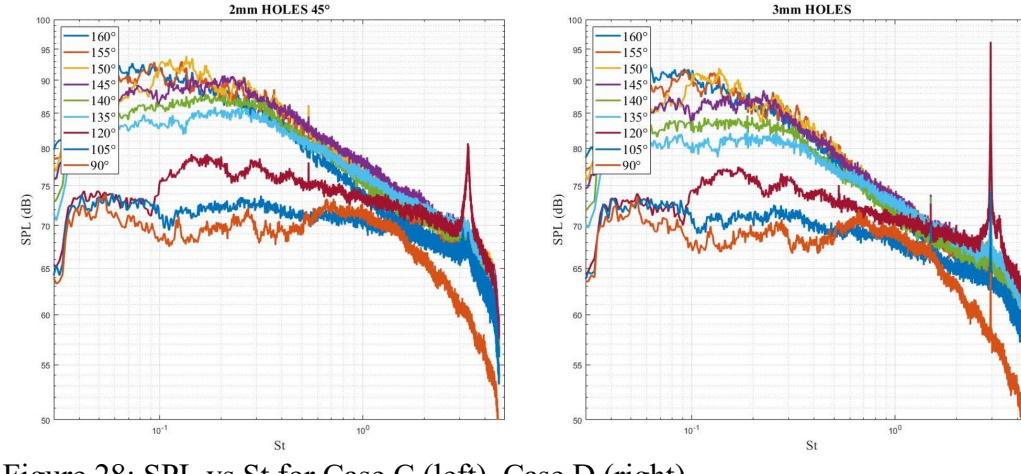

Figure 28: SPL vs St for Case C (left), Case D (right).

Schlieren

The stitched, averaged, schlieren images for all of the test cases can be seen in Figure 29. As the jet plume moves downstream and the turbulence of the system increases (shown by the blurring of shocks in the averaged images), the differences between the cases are minute. Predictably, the largest differences between the cases occur in the near-field near the nozzle exit. Figure 29 shows a zoom into this region with like shock structures color coded to more easily see the differences. The coloring of the shock structures are as follows: Purple corresponds to the lip shock that forms at the end of the expansion ramp as the flow aligns with the free stream. Green corresponds to the reflected shock that originates at the interface of the two flow streams. The Red lines correspond to a series of weak compression waves that originate within the SERN. The Green and Purple shocks meet at a location referred to as the "drill" region during previous analysis. These shocks reflect off the drill region and undergo a merging process to form the Pink shock. The existence of the active control mechanism creates an additional reflected shock that forms at the area of actuation, this shock is highlighted in Orange and is seen in cases B-E. Case B, 2mm holes, saw the introduction of the Orange shock which had little effect on the other shocks of the near field until the drill region. The Orange shock inhibits the Green shocks ability to reach the deck plate surface, this in turn causes the reflected Pink shock and expansion fan to differ from the baseline flow. Case C, 2mm hole at 45 degrees, has the largest effect on the near field shock structures. The Orange shock causes a change in the angle of the Green shock forcing it to interact with the Orange shock before the drill region. This allows the Purple shock to make its way down to the deck surface and increases the size of the drill region. Case D, 3mm holes, appears similar in structure to Case B. In both cases the uppermost Red structure is seemingly blocked by the Orange shock. Finally observing Case E, the full open slot corresponding to the maximum momentum coefficient of the actuation system, the relationship between the Orange and Green shocks is similar to that of cases B and D where air is blown perpendicular to the bulk flow. The largest difference exists in the lip shock as it makes its way toward the drill region and "bows" out near the deck surface. Additionally there is a slight effect on the plume deflection of the jet by the actuated cases. All of the actuated cases saw a minor increase in the plume deflection, although the increased turbulence and lack of clarity in the jet plume after it leaves the deck plate region make quantifying this difference difficult (it can be observed in the raw schlieren videos when pulsing the actuator). It should also be noted that the flow of the jet for all cases is highly 3-Dimensional, so all of the schlieren images do not provide us with a true map of the flow structures, hence their qualitative nature.

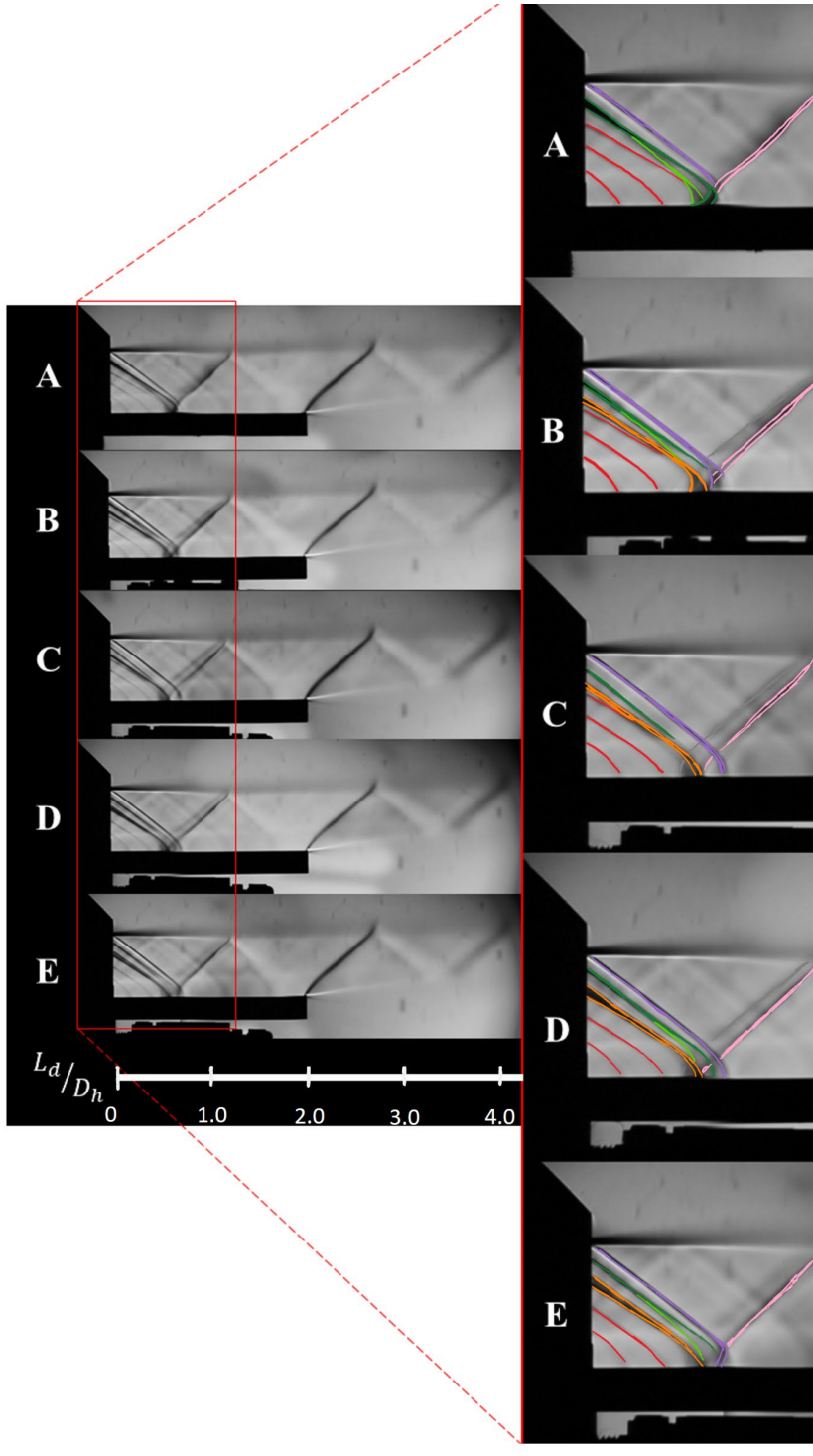

Figure 29: Comparisons of schlieren for test cases. A: baseline flow, B: 2mm holes, C: 2mm holes 45 degrees, D: 3mm holes, E: Full open slot.

Summary of Preliminary Experimental Active Control Results of Full SERN Configuration

In order to build off of the control framework of the passive study, a plan for active control by way of a micro jet array has been laid out and a parametric study into its effects has begun. The introduction of JISCs to a flowfield has been shown to alter the distribution of energy and produce a corrugated shock pattern, similar in structure to the shock pattern created by the wavy SPTE. The addition of a plenum chamber that sits atop the aft deck plate where the redirected bypass flow passes through a converging section will allow for sonic conditions to be achieved by the JISCs to interact with the sonic flow of the third stream at the location where it meets the core stream of the nozzle. A solenoid valve at the inlet of the plenum will allow for unsteady actuation via adjustment of the duty cycle of the current applied to the valve. Four different actuation cases with steady blowing were tested and their respective far-field spectra and averaged schlieren images were compared. For all actuation cases it was observed that the dominant frequency tone was shifted to a lower frequency and an additional reflected shock was formed in the near-field. Jets blowing at a 45 degree angle with respect to the core flow were shone to decrease the SPL of this tone by 8dB in addition to the reduction in frequency. The largest diameter holes (3mm) of the current system blowing air perpendicularly at spacing that correspond to the passive control study was found to amplify this tone by 8dB. These two cases exhibited the largest departure from the baseline flow.

OVERALL SUMMARY

The flow field within the MARS is a highly complex composition of several canonical flows. This flow has been the subject of extensive research over the past decade. In depth experiments and simulations have been conducted in tandem to identify any undesirable effects of the flow from an application based point of view. One of the unique features of the nozzle, its multi stream nature was shown to produce an unwanted effect in the form of a dominant tone traced back to the instability at the interface of the two streams. Resolvant analysis was performed and, based on this analysis, passive control of the system was implemented by way of introducing a spanwise perturbation to the splitter plates trailing edge. In both experiments and LES simulations, this geometric modification was shown to diminish the dominant tone, this energy was distributed elsewhere and several other peaks appeared.

Preliminary active control results, for all actuation cases, showed that the dominant frequency tone was shifted to a lower frequency and an additional reflected shock was formed in the near-field. Jets blowing at a 45 degree angle with respect to the core flow were shone to decrease the SPL of this tone by 8dB in addition to the reduction in frequency. The largest diameter holes (3mm) of the current system blowing air perpendicularly at spacing that correspond to the passive control study was found to amplify this tone by 8dB. These two cases exhibited the largest departure from the baseline flow.

REFERENCES

Berry, M. G., Magstadt, A. S., Glauser, M. N., Ruscher, C. J., Gogineni, S. P., and Kiel, B. V., "An acoustic investigation of a supersonic, multi-stream jet with aft deck: Characterization and acoustically-optimal operating conditions," *54th AIAA Aerospace Sciences Meeting*, 2016, p. 1883.

Berry, M. G., "Investigating the Interaction of a Supersonic Single Expansion Ramp Nozzle and Sonic Wall Jet," Ph.D. thesis, Syracuse University, 2017.

Berry, M., Magstadt, A., and Glauser, M. N., "Application of POD on time-resolved schlieren in supersonic multi-stream rectangular jets," *Physics of Fluids*, Vol. 29, No. 2, 2017, p. 020706.

Berry, M. G., Stack, C. M., Magstadt, A. S., Ali, M. Y., Gaitonde, D. V., and Glauser, M. N., "Low-dimensional and data fusion techniques applied to a supersonic multistream single expansion ramp nozzle," *Physical Review Fluids*, Vol. 2, No. 10, 2017, p. 100504.

Bruening, G. B., and Chang, W. S., "Cooled cooling air systems for turbine thermal management," *ASME Paper*, Vol. 14, 1999, p. V003T01A002.

Parshwanath S. Doshi, ``Modal Description and Passive Control of a Shear Layer'', Ph.D. Thesis The Ohio State University, 2023

Parshwanath S. Doshi, Rajesh Ranjan, Qiong Liu and Datta V. Gaitonde, Emma D. Gist and Mark N. Glauser, ``Toward a Passive Control Strategy for a Supersonic Multi-Stream Flow using Resolvent Analysis'', AIAA SciTech Meeting, January 2021a, AIAA 2021-1557.

Parshwanath S. Doshi, Datta V. Gaitonde, Emma D. Gist and Mark N. Glauser, `` Passive Control of a Supersonic Shear Layer in a Rectangular Multi-Stream Jet'', AIAA Journal 2022.

Gist, E., "Exploring Passive Flow Control Techniques Applied to a Supersonic Multistream Rectangular Nozzle'', Ph.D. Thesis, Syracuse University, 2022.

Gist, E., Doshi, P., Kelly, S., Glauser, M., and Gaitonde, D., "Exploratory Passive Flow Control Study of a Supersonic MultiStream Nozzle Flow," AIAA-2020-2952.

Emma Gist, Seth Kelly, Rishov Chatterjee, Parshwanath Doshi, Mark Glauser and Datta Gaitonde, ``Spanwise Wavenumber Perturbation on a Splitter Plate in a Rectangular Supersonic Nozzle'', AIAA Scitech Meeting, January 2022, San Diego California, AIAA 2022 –

Emma D. Gist, Rishov Chatterjee, Mark N. Glauser, Parshwanath S. Doshi and

Datta V. Gaitonde, ``Splitter Plate Sinusoidal Serrations for Passive Control of a Rectangular Multi-Stream Supersonic Jet'', In Review, AIAA Journal (Submitted December 2021b).

Emma D. Gist, Seth W. Kelly, Tyler M. Vartabedian, Rishov Chatterjee, Parshwanath S. Doshi, Mark N. Glauser and Datta V. Gaitonde, `` Effects of Geometric Modifications on a Complex Multi-Stream Supersonic Rectangular Nozzle'', AIAA SciTech Meeting, January 2021a, AIAA 2021-1559

Hussain, A. F., "Coherent structures and turbulence," Journal of Fluid Mechanics, Vol. 173, 1986, pp. 303–356.

Kelly, S. and Glauser, M., "Active Control of a Multi-Stream Rectangular Supersonic Nozzle via Micro Jet Array'', AIAA SciTech Meeting, January 2023, AIAA 2023-0851

Seth W. Kelly, Tyler M. Vartabedian, Emma D. Gist, and Mark N. Glauser, ``Neural Network Noise Prediction for a Complex Supersonic Rectangular Jet Nozzle'', AIAA SciTech Meeting, January 2021, AIAA 2021-1691

Magstadt, A., Berry, M., Shea, P., Glauser, M., Ruscher, C., Gogineni, S., and Kiel, B., "Aeroacoustic experiments on supersonic multi-aperture nozzles," *53rd AIAA/ASME/SAE/ASEE Joint Propulsion Conference*, Orlando, FL, 2015.

Magstadt, A. S., "Investigating the Structures of Turbulence in a Multi-Stream, Rectangular, Supersonic Jet," Ph.D. thesis, Syracuse University, 2017.

Magstadt, A. S., and Glauser, M. N., "Stereo PIV Measurements in a Multi-stream, Rectangular, Supersonic Jet," *2018 AIAAAerospace Sciences Meeting*, 2018, p. 0054.

Papamoschou, D., and Debiasi, M., "Directional suppression of noise from a high-speed jet," *AIAA journal*, Vol. 39, No. 3,2001, pp. 380–387.

Ruscher, C. J., Gogineni, S., and Ferrill, T., "Splitter Plate Edge Effects in a Supersonic Multi-stream Nozzle," 2018 Joint Propulsion Conference, 2018, p. 4745.

Simmons, R. J., "Design and control of a variable geometry turbofan with and independently modulated third stream," Ph.D. thesis, The Ohio State University, 2009.

Stack, C. M., Adler, M. C., and Gaitonde, D. V., "Influence of the Splitter Plate Thickness on the Near-Wake Dynamics of Compressible Turbulent Mixing Layers," AIAA Scitech 2019a Forum, 2019, p. 1877.

Stack, C. M., and Gaitonde, D. V., "Shear Layer Dynamics in a Supersonic Rectangular Multistream Nozzle with an Aft-Deck," *AIAA Journal*, Vol. 56, No. 11, 2018, pp. 4348–4360.

Stack, C. M., and Gaitonde, D. V. (2017), "Dynamical features of a supersonic multistream nozzle with an aft-deck," *55th AIAA aerospace sciences meeting*, p. 0557.

Stack, C. M., and Gaitonde, D. V. (2018), "Mechanisms Influencing Surface Pressure Unsteadiness on the Aft-Deck of a Rectangular Multistream Supersonic Nozzle," *2018 AIAA Aerospace Sciences Meeting*, p. 0822.

Stack, C. M. (2019), "Turbulence Mechanisms in a Supersonic Rectangular Multistream Jet with an Aft-Deck," Ph.D. thesis, The Ohio State University.